Deconvoluting the Magnetic Structure of the Commensurately Modulated Quinary Zintl Phase $Eu_{11-x}Sr_xZn_4Sn_2As_{12}$

Kasey P. Devlin,[†] Junjie Zhang,[‖] James C. Fettinger,[†] Eun Sang Choi,[^] Ashlee K. Hauble,[†] Valentin Taufour,[‡] Raphael P. Hermann,[‖] and Susan M. Kauzlarich*[†]

[†]Department of Chemistry, University of California, One Shields Avenue, Davis, California 95616, United States

[‖]Materials Science and Technology Division, Oak Ridge National Laboratory, Oak Ridge, Tennessee, 37831, United States

[^]National High Magnetic Field Laboratory, Tallahassee, FL, 32310, United States

[‡]Department of Physics and Astronomy, University of California, One Shields Avenue, Davis, California 95616, United States

ABSTRACT

The structure, magnetic properties, and ^{151}Eu and ^{119}Sn Mössbauer spectra of the solid-solution $Eu_{11-x}Sr_xZn_4Sn_2As_{12}$ are presented. A new commensurately modulated structure is described for $Eu_{11}Zn_4Sn_2As_{12}$ ($R\bar{3}m$ space group, average structure) and is closely resembling the original structural description in the monoclinic $C2/c$ space group with layers of Eu, puckered hexagonal Zn_2As_3 sheets, and Zn_2As_6 ethane-like isolated pillars. The solid-solution $Eu_{11-x}Sr_xZn_4Sn_2As_{12}$ ($0 < x < 10$) is found to crystallize in the commensurately modulated $R\bar{3}$ space group, related to the parent phase but lacking the mirror symmetry. $Eu_{11}Zn_4Sn_2As_{12}$ orders with a saturation plateau at 1 T for 7 of the 11 Eu^{2+} ions ferromagnetically coupled (5 K) and shows colossal magnetoresistance at 15 K. The magnetic properties of $Eu_{11}Zn_4Sn_2As_{12}$ are investigated at higher fields, and the ferromagnetic saturation of all 11 Eu^{2+} ions occurs at ~ 8 T. The temperature-dependent magnetic properties of the solid-solution were investigated, and a non-trivial structure-magnetization correlation is revealed. The temperature-dependent ^{151}Eu and ^{119}Sn Mössbauer spectra confirm that the europium atoms in the structure are all Eu^{2+} and that the tin is consistent with an oxidation state less than four in the intermetallic region. The spectral area of both Eu(II) and Sn increase at the magnetic transition, indicating a magnetoelastic effect upon magnetic ordering.

INTRODUCTION

Eu containing Zintl phases are of interest for their wide variety of structures and resulting magnetic and transport properties.[1–5] In many cases, these compounds can be considered small band gap ferromagnetic semiconductors and show colossal magnetoresistance (CMR) behavior. Many Zintl phases have also been shown to have excellent thermoelectric properties, such as Eu_2ZnSb_2[6,7] and $EuZn_2Sb_2$.[8] The high efficiency of the thermoelectric properties for Eu_2ZnSb_2 are attributed to the low lattice thermal conductivity and high mobility.[7] While antimony-containing Zintl phases substituted with Eu on the cation site show a variety of magnetic ordering and magnetoresistance behavior,[1,9] arsenic-containing Zintl phases typically have larger band gaps and are less likely to show magnetic ordering. Arsenic containing examples of magnetically-coupled Eu^{2+} ions include $Eu_{14}MnAs_{11}$ (T_c = 74 K),[9] $Eu_5Sn_2As_6$ (T_c = 30 K),[10] and $EuIn_2As_2$ (T_N = 16 K).[11] A new Zintl phase, $Eu_{11}Zn_4Sn_2As_{12}$, was recently shown to exhibit CMR with a maximum reduction at 15 K by ~3000-fold at 9T. Magnetic polarons have been suggested as a possible mechanism for the observed CMR.[12] Additionally, the magnetization versus field data indicates that while most of the Eu^{2+} are ferromagnetically ordered at 1 T (7 of the 11 Eu^{2+}), full saturation of all 11 Eu^{2+} does not occur up to 7 T.[13]

The $Eu_{11}Zn_4Sn_2As_{12}$ crystallizing in the monoclinic space group, *C*2/*c*, has been described as consisting of layers stacked in the crystallographic *c* direction and is shown in **Figure 1**.[13] The layers can be separated into three types based on their chemical bonding: layers of pseudo-hexagonally packed Eu^{2+} cations (**A**), sheets of $^2_\infty[Zn_2As_3]^{5-}$ (**B**), and layers of $[Sn_2As_6]^{12-}$ pillars (**C**). The anionic layer of $^2_\infty[Zn_2As_3]^{5-}$ (**B**) forms a 2-D defect containing hexagonal net. The sheets of **A** and **B** are somewhat undulated or puckered, therefore not perfectly flat. There are two slightly different arrangements of Eu atoms within the monolayer represented as $\mathbf{A_i}$ and $\mathbf{A_{ii}}$ layers. The remaining two Eu^{2+} cations sit between the isolated Sn_2As_6 pillars to balance the charge and are considered a part of the layer **C**; these pillars are described as ethane-like units in a staggered configuration. Overall, a stacking sequence of $\mathbf{A_i - B - A_{ii} - C - A_{ii}(2) - B(2) - A_i(2) - \overline{B(2)} - \overline{A_{ii}(2)} - \overline{C} - \overline{A_{ii}} - \overline{B} - \overline{A_i}}$ describes the unit cell, where **(2)** stands for an equivalent layer produced by a 2-fold axis, and the bar symbol denotes a layer generated by inversion.

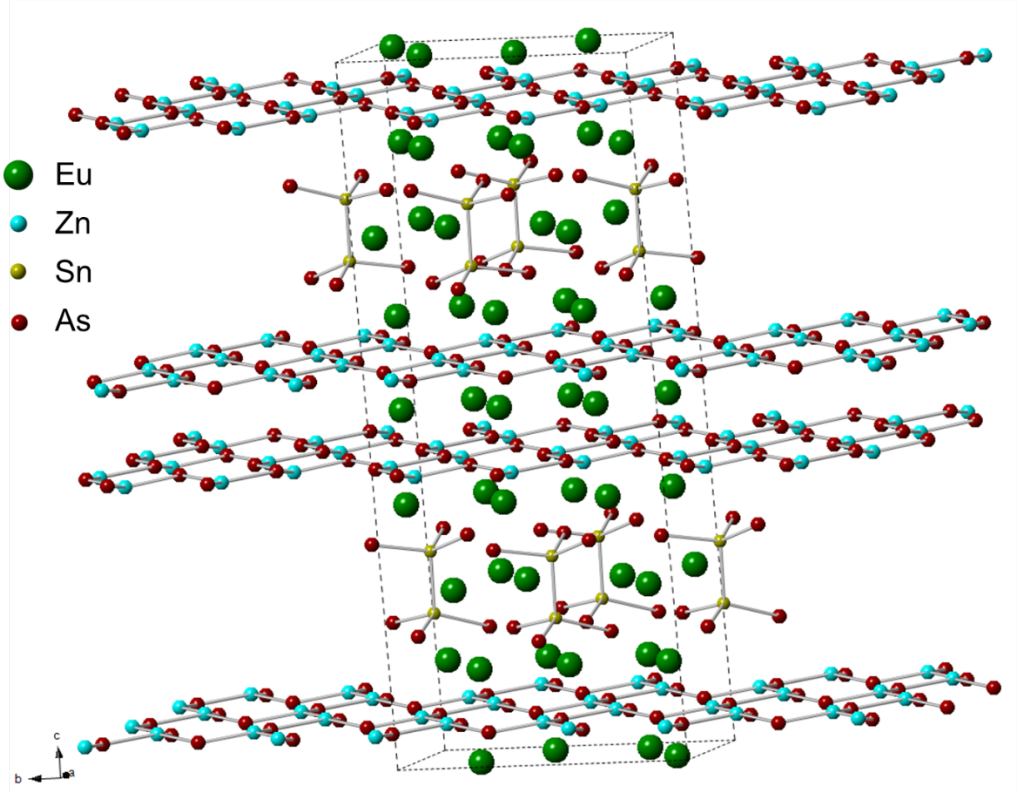

Figure 1. A view of the monoclinic crystal structure (Space group *C*2/*c*) of $Eu_{11}Zn_4Sn_2As_{12}$ where Eu is indicated in green, Zn in cyan, Sn in yellow, and As in red.

Following the classic Zintl-Klemm electron counting rules,[14,15] $Eu_{11}Zn_4Sn_2As_{12}$ can be considered a Zintl phase because it can be described in terms of discrete $[Sn_2As_6]^{12-}$ pillars with four-bonded Sn^0 and one-bonded As^{2-}, sheets of $^2_\infty[Zn_2As_3]^{5-}$ with two-bonded As^{1-} and three-bonded Zn^{1-}, and isolated Eu^{2+} cations. This bonding description represents a valence precise compound as the following electron counting calculation shows: $Eu_{11}Zn_4Sn_2As_{12}$ = 11 Eu^{2+} x 2 $[Zn_2As_3]^{5-}$ x $[Sn_2As_6]^{12-}$. Electronic structure calculations are in agreement with the electron counting and indicate that this compound is a small bandgap semiconductor.[13] The structure does not contain any As-As bonds, and the arsenic atoms can be assigned their lowest oxidation number of -3. Considering that there is a homoatomic Sn–Sn bond in the Sn_2As_6 motif (staggered ethane-like), it can be written as $[Sn_2]^{6+}$, which provides a formal oxidation state of +3 for each tin. Finally, the metal atoms can be assigned with their oxidation numbers of +2 for both europium and zinc. This model for chemical bonding of a two-electron, two-center bond for Sn_2 and the polar Sn−As covalent bonding within $[Sn_2As_6]^{12-}$ units is supported by electron localization function (ELF) calculations.[13] These isolated Sn_2As_6 ethane-like units are rare[16,17] but have been observed in the chiral Zintl phases, $A_{14}Sn_3As_{12}$ (A = Sr, Eu).[18] The $^2_\infty[Zn_2As_3]^{5-}$ layer of the $Eu_{11}Zn_4Sn_2As_{12}$

structure is similar to that found in Sr_2ZnAs_2 (space group $P6_3/mmc$)[19] which is described as a highly-symmetric hexagonal unit cell in which the vacancies are randomly distributed on the Zn site. A pair distribution function (PDF) analysis of the analog, Eu_2ZnBi_2, suggested an ordered super-structure with lower symmetry (space group C2/c) with variation of the Zn–Bi bond angle and corrugation of the nominally planar hexagonal layer.[6] The Eu_2ZnSb_2 phase has received significant recent attention for its high mobility and excellent thermoelectric properties.[6,20]

This work presents a new commensurately modulated structural description of the $Eu_{11}Zn_4Sn_2As_{12}$ compound and the structure and properties of the solid solution, $Eu_{11-x}Sr_xZn_4Sn_2As_{12}$, may also be described as a commensurately modulated structure. Probing the magnetic properties by substituting Sr^{2+} for Eu^{2+} provides insight into the coupling, unusual magnetization, and transport properties. In addition, the magnetic properties under high fields, the magnetic properties of the $Eu_{11-x}Sr_xZn_4Sn_2As_{12}$ solid-solution, and the Mössbauer spectra of Eu and Sn are presented.

EXPERIMENTAL

Synthesis

All manipulations were carried out in an argon-filled glove box. The growth of $Eu_{11-x}Sr_xZn_4Sn_2As_{12}$ single crystals was adapted from the reported synthesis of $Eu_{11}Zn_4Sn_2As_{12}$.[13] The elements were loaded in 5 mL alumina crucible set[21] in the respective Eu:Sr:Zn:As:Sn molar ratios of (11-x):x:6:12:95 to a total weight of 5 g; (Sources: Eu metal pieces, Ames Lab, 99.999%; Sr metal pieces, Aesar, 99%; Zn powder, Alfa, 99.98%; As chips, Johnson Matthey Chemicals, 99.9999%; and Sn shot, Alpha Aesar, 99.99%). The crucible set was placed into a fused silica tube and sealed under less than 100 mTorr of vacuum. The sealed tube was placed upright in a box furnace, surrounded by fire brick, and heated at 200 ˚C/h to 650 ˚C, allowed to dwell for 1 h, and then heated at 200 ˚C/h to 875 ˚C. The reaction vessel was immediately cooled to 800 ˚C and allowed to dwell for 1 hr. The reaction vessel was slowly cooled at 2 ˚C/h to 500 ˚C. Once at 500 ˚C, the sample was heated at 200 ˚C/h to 650 ˚C, at which point molten tin was removed by centrifuging. Silver-colored, reflective, block-like crystals of $Eu_{11-x}Sr_xZn_4Sn_2As_{12}$ were observed as the product by opening the reaction vessels in an Ar-filled glove box equipped with an optical microscope and at moisture levels below 1 ppm. Single phase product was never achieved, and the best synthesis results in a mixture of crystals of $Eu_{11-x}Sr_xZn_4Sn_2As_{12}$, $EuZn_2As_2$, and $Eu_5Sn_2As_6$. The presence of these three phases was confirmed via unit cell determination of single crystals. The crystals were separated by morphology. The large crystals were $Eu_{11-x}Sr_xZn_4Sn_2As_{12}$, and the remaining small crystals were a mixture of $EuZn_2As_2$ and $Eu_5Sn_2As_6$. A

full Sr analog, $Sr_{11}Zn_4Sn_2As_6$, was synthesized, and the morphology was as expected for the correct phase. However, due to the increasing air sensitivity of the $Sr_{11}Zn_4Sn_2As_6$ crystals, single crystal data were not collected.

Polycrystalline samples were mechanically milled to homogenize the elements and synthesized via annealing. Prior to milling, elemental Eu (Ames Lab, 99.999%) was brushed to remove oxide and cut into pieces along with As chips (Johnson Matthey Chemicals, 99.9999%) and combined on stoichiometry with Zn powder (Alfa, 99.98%) and Sn shots (Alpha Aesar, 99.99 %) to a total weight of 3 g in an argon-filled glove box. The 3 g mixture was then loaded into a 5 mL tungsten carbide ball-mill with two tungsten carbide balls and sealed with an O-ring, tungsten carbide disks, and Teflon caps. The end caps were secured with electrical tape, and then the canister was heat-sealed into two poly bags and placed in a SPEX 8000 M for 30 minutes, transferred to a glovebox and scraped with a metal chisel, resealed, and milled for an additional 30 minutes. The resulting powder was sealed in a Nb tube with an argon-filled arc welder. The tube was then sealed into an evacuated silica jacket and placed in a box furnace to be annealed 565 ˚C for 7 days. The annealed powder was ground with an agate mortar and pestle, sieved through a 100-mesh sieve, loaded into a 12.7 mm diameter graphite die, and sintered using a Dr. Sinter Jr. SPS instrument. The density of the resulting pellet was 5.95 g/cm^3, >90% of the theoretical density.

Single Crystal X-ray Diffraction

Data processing

In all cases, data collected were corrected for Lorentz and polarization effects with Saint[22] and absorption using Blessing's method and merged as incorporated with the program Sadabs.[23,24] The SHELXTL[25] program package was implemented to determine the probable space group and set up the initial files.

$Eu_{11-x}Sr_xZn_4Sn_2As_{12}$ (x = 1, 2, 4, 6, and 9)

Silver, block-like crystals were placed and optically centered on the Bruker[26] Venture Dual source Kappa Photon100 diffractometer at T = –173° C (100 K) under a cold stream of nitrogen and data collected with Mo Kα (λ = 0.71073 Å) radiation. Data were collected with 0.3° wide scans, variable time per frame dependent upon detector 2θ angle and varying φ and omega angles such that nearly all unique reflections were collected at least once.

The first structure in this series (x = 1) had its structure determined via a novel approach. The unit cell was initially determined with the Bruker software APEX3 package[26] and found to be

monoclinic C with many weak reflections present. JANA2006 was then implemented and indicated the unit cell was monoclinic C when using all of the reflections present and rhombohedral R when only the strong reflections were used for unit cell determination producing a modulation vector of q = 1/3, 1/3, 1/2. Data were processed for the rhombohedral setting.

The hexagonal setting data were integrated with the determined q-vector. Since the q-vector had a rational fraction and no super space groups exist for it, an absorption correction was applied to obtain a HKLF4 file that was further input into XPREP, processed normally, and the output $R\bar{3}$ (no.148) was the suggested space group. The structure was initially determined with XT[27] but none of the actual atom types were identified. The structure determination proceeded as follows. All of the atoms were initially input as Eu with a similar thermal parameter instruction input for all of the atoms (SIMU) and their occupancies were allowed to refine. The overall residuals for the structure converged well but what was on each site was yet to be determined. After some analysis, the Eu and Sn atoms shared sites and those near one another, along with As, Sn and Zn atom sites began to emerge. The amount of Zinc in each unit of composition is 4 (as determined from EMPA of the single crystals), creating a basis set for the rest. A series of equations (SUMP) were input to both refine the relative amounts of each atom present on shared or nearby sites and to also charge balance to zero. A large damping instruction (DAMP) was input to allow for the various atom sites and overall charge balance to converge slowly. Upon convergence, the DAMP instruction was then reduced, additional refinement and finally removed such that the overall composition and charge were allowed to converge and become zero, respectively. The structure was carefully analyzed, the final cell contents updated, and the final refinement undertaken.
The remaining structures, x = 2, 4, 6, and 9, were refined in the following manner. The modulation vectors of x = 2, 4, 6, and 9 were q = 1/3, 1/3, 1/2 were determined from JANA2006. Starting with the atom positions from x = 1 input into the starting instruction file, a similar process as described above was followed until complete convergence. Single crystal X-ray diffraction data collections and refinement parameters (including q, the modulation vector). are provided in **Table S1**. Atomic coordinates for the compositions are listed in **Table S2**.

$Eu_{11}Zn_4Sn_2As_{12}$

A silver, block-like crystal was placed and optically centered on the Bruker[22] APEXII CCD system at 90 K. Indexing of the unit cell used a random set of reflections collected from three series of 0.5° wide ω-scans, 10 seconds per frame, and 30 frames per series that were well-distributed in reciprocal space. Four ω-scan data frame series were collected [Mo K_α] with 0.3° wide scans, 20

seconds per frame, and 606 frames collected per series with the detector set at 32.0° at varying φ angles (φ = 0°, 90°, 180°, 270°). The crystal detector distance was 5.00 cm, thus providing a complete sphere of data to $2\theta_{max}$ = 54.96°.

Using JANA2006, only about 10% of the reflections led to the rhombohedral setting. $Eu_{11}Zn_4Sn_2As_{12}$ also possessed a mirror plane and was determined in *R*-3*m* (no. 166). The structure was determined by direct methods using the program XT[27] using the refined R-3 structure solution positional parameters with the occupancy set to half to account for the mirror plane with q = 2/3, 2/3, 0. The structure was refined with XL employing all reflections.[28] The Sn and Zn site occupancies converged to 1/3 and 2/3 occupancy, respectively. After the site occupancy converged, the occupancies were set and not refined further. The final structure was refined to convergence, and the final difference-Fourier map was featureless, indicating that the structure is both correct and complete. An empirical correction for extinction was also determined and applied.s

CSD 2052235-2052240

$Eu_{11}Zn_4Sn_2As_{12}$ (CSD 2052236) has B level alerts regarding residual density around heavy atoms. The residual intensity surrounding Eu2 is attributed to truncation errors in the data, or small deviations in the unit cell alignment.

$Eu_{7.92}Sr_{3.08}Zn_4Sn_2As_{12}$ (2052239) and $Eu_{1.48}Sr_{9.52}Zn_4Sn_2As_{12}$ (2052237) have B level alerts regarding residual density around heavy atoms. The residual density is attributed to the nature of the compound, substitution that is present, the modulation, and the likelihood that not all unit cells are perfectly aligned.

Powder X-ray Diffraction (PXRD)

PXRD patterns were collected on pre-consolidated powder using a Bruker D8 Advance X-ray diffractometer utilizing Cu Kα radiation in the 2θ range 10˚ - 80˚ with a step size of 0.02˚ operated at 40 KV and 25 mA. Rietveld refinements of the data were performed using GSAS-II[29] to determine unit cell parameters and weight percentages of any impurity phases present.

Electron Microprobe Analysis (EMPA)

Multiple single crystalline samples of each composition were chosen from each reaction batch, enclosed in epoxy, and polished to provide flat surfaces for analysis. The polished samples were carbon coated. Microprobe analysis was performed by using a Cameca SX-100 Electron Probe Microanalyzer with five wavelength-dispersive spectrometers (WDS). Compositions of samples

were determined from the X-ray intensities of the elements Eu, Sr, Zn, As, and Sn, employing the calibrated standards of $EuPO_3$, $SrTiO_3$, Zn (metal), GaAs, and Sn (metal) for quantitative analysis. The composition of each sample was determined by calculating the average and standard deviation of at least 10 randomly selected data points from a single crystal and restraining the total atoms to 29; however, for the compositional stoichiometries of $Eu_{11-x}Sr_xZn_4Sn_2As_{12}$ where $x > 5$, the crystals appeared to be air sensitive, and an oxide coating developed. The compositions of samples with $x > 5$ were determined by assuming that the composition is a two-component system, $Eu_{11-x}Sr_xZn_4Sn_2As_{12}$ solid solution, and the oxide, SrO. Therefore, the composition of $Eu_{11-x}Sr_xZn_4Sn_2As_{12}$ solid solution is normalized to As = 12, the Eu content was calculated as x, and the Sr was assumed to be 11-*x*. Any additional Sr was assumed to be oxide, SrO.

Thermogravimetry/Differential Scanning Calorimetry (TG/DSC)

Data were collected by a Netzsch STA 449 F3 using the SiC furnace. After the baselines were established, a single crystal of $Eu_{11}Zn_4Sn_2As_{12}$ was loaded into an alumina crucible. The sample was heated from room temperature to 1100˚C under 50 mL/min argon flow at a heating rate of 3 K/min. TG/DSC showed an initial melting point of 1126 K and decomposition temperature of ~1200 K, **Figure S1**. This melting point was used as a starting point for metallurgical synthesis, described above.

Magnetism

The crystal of each composition that resulted in the most homogenous dispersion of Eu/Sr and was free of Sn inclusions from the EMPA backscattered images was selected for magnetic measurements and removed from epoxy with dichloromethane. Single crystal X-ray diffraction data was collected to confirm the structure type before placing the crystals in epoxy, and the resulting composition was compared to the EMPA crystal with the most homogenous dispersion of Eu/Sr, **Table S3** and **Figure S2**. A polycrystalline sample was also measured. A 1 x 1 x 1 mm^3 cube was cut from the fully-dense, spark plasma sintered pellet and characterized by PXRD, **Figure S3**. The Rietveld refinement results are summarized in **Table S4**. Zero-field-cooled (ZFC) and field-cooled (FC) magnetization data were collected in a Quantum Design Magnetic Properties Measurement System (MPMS) from 300 to 2 K and up to 7 T. The single crystals presented were aligned with the magnetic field parallel to the longest axis which is verified to be the *c* axis by indexing the crystal faces.

AC Susceptibility and Resistivity Measurements

AC susceptibility measurements were taken at the National High Magnetic Field Laboratory in Tallahassee, FL on the SCM2 utilizing a home-made ac susceptometer.[30] The field dependence of the ac susceptibility of $Eu_{11}Zn_4Sn_2As_{12}$ was measured by sweeping DC fields from -18 T to 18 T (0.3 T/min) at 2 K, 5 K, 8 K, 11 K, and 30K. The crystal was packed into a Kapton tube with epoxy. The amplitude and the frequency of the ac-field were 3.2 Oe and 80 Hz, respectively.

For resistance measurements, 5 gold wire leads were attached to previously polished crystals with silver paint. Currents of 0.5 μA and 10 μA were used for data collection for a polycrystalline sample and single crystal sample, respectively, from T = 2 K to 300 K. All single crystals were selected by morphology and the unit cell was confirmed by single crystal XRD.

Mössbauer Spectroscopy

Single crystal and the polycrystalline samples were measured. The single crystalline samples were visually inspected for the correct phase, and the surfaces of the crystals were scraped with a razor blade to remove the excess Sn-flux. The samples were ground into powders in an Ar-filled glovebox. 70 mg of powdered samples were mixed with boron nitride after being sifted through a 325-mesh sieve and sandwiched between Kapton tape in the sample holder. ^{151}Eu and ^{119}Sn Mössbauer spectra were acquired with a 50 mCi $^{151}SmF_3$ and a 10 mCi $Ca^{119m}SnO_3$ source, respectively. The samples were placed in a Janish SHI-850-HT closed cycle cryostat; the velocity transducer was operated in constant acceleration mode and calibrated using the room-temperature α-iron Mössbauer spectrum with a ^{57}Co@Rh source. Isomer shifts are reported relative to EuF_3 and $CaSnO_3$.

Results and Discussions

$Eu_{11}Zn_4Sn_2As_{12}$ was initially prepared via flux growth single crystals. Single crystals of $Eu_{11-x}Sr_xZn_4Sn_2As_{12}$ were synthesized in a similar manner in order to probe the relationships between the crystal structure and magnetic properties of the parent $Eu_{11}Zn_4Sn_2As_{12}$ compound, while polycrystalline $Eu_{11}Zn_4Sn_2As_{12}$ was synthesized to confirm the results of the single crystal measurements.

Crystal Structure

Single crystal diffraction data of $Eu_{11-x}Sr_xZn_4Sn_2As_{12}$ were collected on crystals from reactions where the experimentally loaded stoichiometric amounts of Sr were 0, 1, 2, 4, 6, and 9. The refined compositions were determined to be $Eu_{11-x}Sr_xZn_4Sn_2As_{12}$ (x = 0, 1.69, 2.06, 3.08, 4.83, and 9.52).

Based on Laue symmetry and systematic absences, the structures of $Eu_{11-x}Sr_xZn_4Sn_2As_{12}$ ($x > 0$) are best described in a centrosymmetric, rhombohedral structure crystallizing in the space group $R\bar{3}$ (No. 148) with 8 atoms per unit cell. Additionally, the structures are commensurately modulated structures by inspecting the diffraction pattern (wavevectors provided in Table S1). The structure solution for $Eu_{11}Zn_4Sn_2As_{12}$ was reinvestigated and was determined to be better described as a commensurately modulated structure in the $R\bar{3}m$ space group (No. 166).

The structures crystallizing in the $R\bar{3}m$ and $R\bar{3}$ space groups, hereafter referred to as the $R\bar{3}m$ or $R\bar{3}$ structure. have the same hexagonal unit cell parameters and are described by linearly increasing unit cell parameters with the addition of Sr, **Figure 2**. The structures are nearly identical with only the loss of mirror planes and 2-fold rotation axes distinguishing the two space groups. The $R\bar{3}m$ structure contains 7 crystallographically unique positions comprised of three Eu, one Sn, two As, and one Zn site. Similarly, the $R\bar{3}$ structures contain 8 crystallographically unique positions with the same sites for Eu, Sn, As, and Zn along with one additional Sr site. The Eu1 (Eu1/Sr1) atom is located on the Wyckoff 3b site and Eu2, As4, As5, Zn6, and Sn7 atoms all occupy the 6c site, Eu3 occupies the 3a site, and Sr2, existing only in the $R\bar{3}$ structures, occupies the 18f site. The Eu/Sr occupancies from the refinements are in reasonable agreement with the EMPA compositions provided in **Table S3**. The slight variation in stoichiometry results from minor compositional deviation between crystals in the same batch.

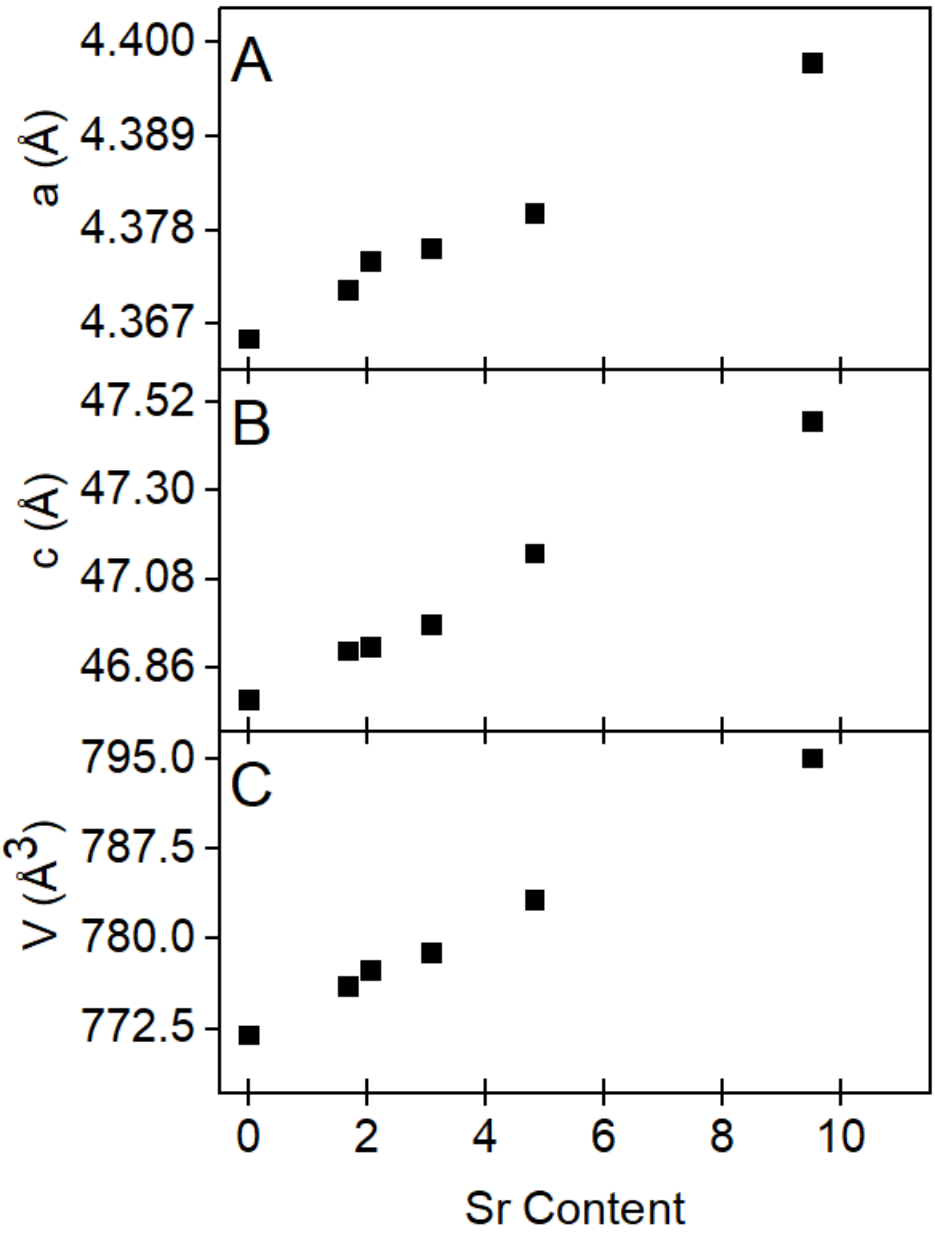

Figure 2. Rhombohedral lattice parameters, from Table S1, for $Eu_{11-x}Sr_xZn_4Sn_2As_{12}$ (90(2) K; $R\bar{3}m$ (x = 0) and $R\bar{3}m$ ($x \geq 0$)) as a function of Sr content from single crystal refinement. (A) a – axis, (B) c – axis, and (C) Volume.

Figure 3 illustrates the $x = 0$ and solid solution structure for $Eu_{11-x}Sr_xZn_4Sn_2As_{12}$ in the $R\bar{3}m$ ($x = 0$) and $R\bar{3}$ ($x > 0$) space groups, respectively. The layers within the $R\bar{3}m$ and $R\bar{3}$ structures closely resemble the layers described in the original monoclinic $C2/c$ structure[13] and are stacked along the crystallographic c direction. The description of the layers can be expanded into four major types with two different layers of Eu cations (**A**$_i$ and **A**$_{ii}$), sheets of $[Zn_2As_3]^{5-}$ (**B**), and layers of $[Sn_2As_6]^{12-}$ isolated pillars (**C**). Two types of Eu atom arrangements within the monolayer sheets are shown by **A**$_i$ (Eu1) and **A**$_{ii}$ (Eu2) layers (the additional Eu atoms (Eu3) are part of the **C** layer). In **Figure 3,** the isolated pillars appear connected in layer (**C**) because the Sn and Eu sites are shown as fully occupied. The Sn and Eu3 positions cannot be filled at the same time, and the occupational disorder will be discussed in detail below. The Eu atoms are designated by different colors to illustrate the 3 Eu sites in the structure. Although **Figure 3** does not explicitly show vacancies in the Sn and Zn sites, it is present, and the site occupancies were allowed to refine and converged to 1/3 and 2/3, respectively. In the $R\bar{3}$ structure of the solid solution, it is clear that there is disorder of the cation site (Eu2/Sr2) shown in light green. There are multiple ways to describe the relationships between the layers in these rhombohedral structures utilizing 3-fold rotary-inversion elements and/or an inversion center, one such description will be discussed herein.

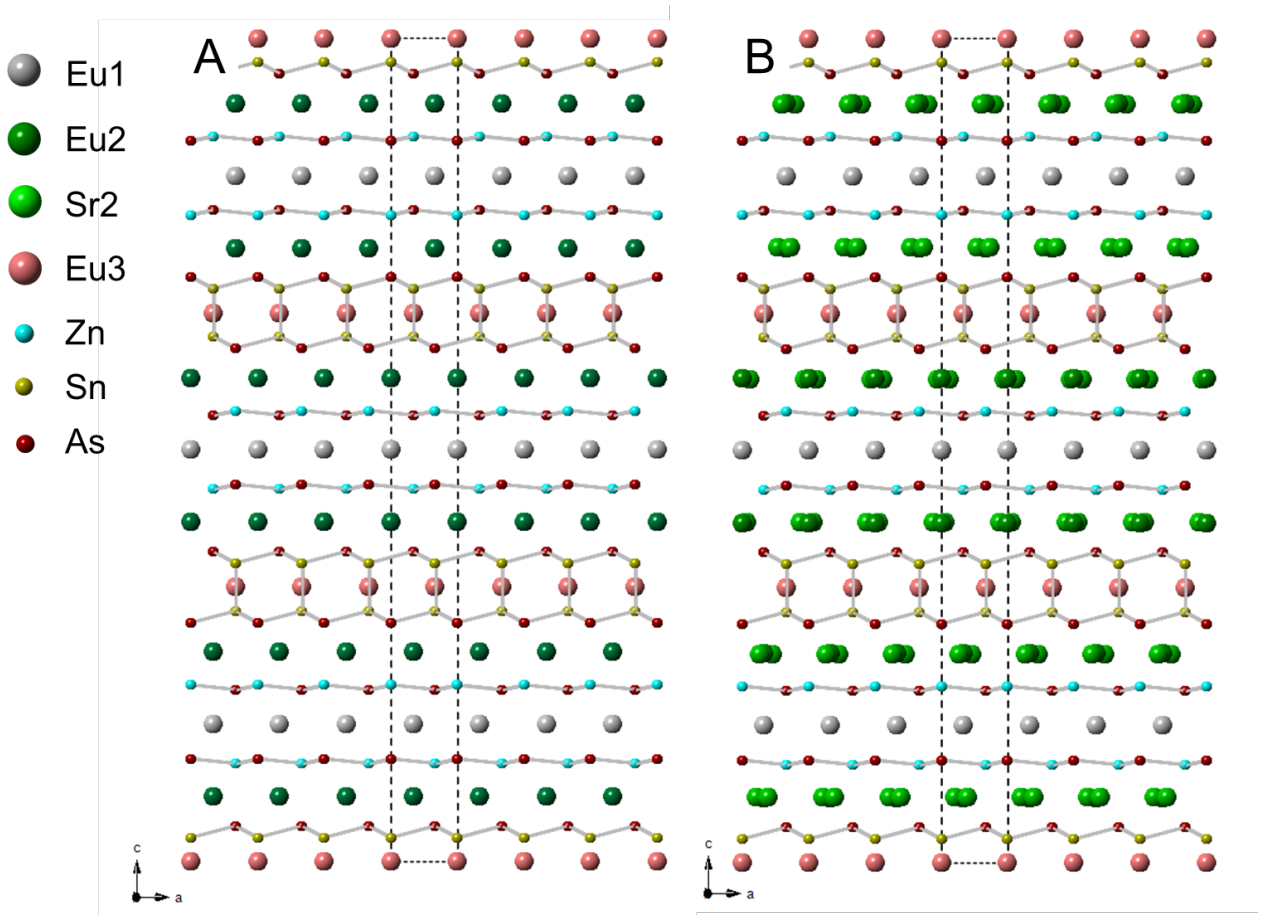

Figure 3. Crystal structures of (A) $Eu_{11}Zn_4Sn_2As_{12}$ in the $R\bar{3}m$ space group and (B) $Eu_{11-x}Sr_xZn_4Sn_2As_{12}$ ($x > 0$) in the $R\bar{3}$ space group projected along the *b* – axis where the Eu sites, Eu1, Eu2, Eu3, are distinguished by the colors, grey, green, and pink, respectively. The additional Sr2 substitution site in $Eu_{11-x}Sr_xZn_4Sn_2As_{12}$ is indicated in light green. The Zn atoms are indicated by the color cyan, the Sn atoms are yellow, and the As atoms are red.

Figure 4 compares the layers of the $Eu_{11-x}Sr_xZn_4Sn_2As_{12}$ structure in the $R\bar{3}m$, $R\bar{3}$, and *C*2/*c* space groups. The $\boldsymbol{A_i}$ layers in the $R\bar{3}$ have the most distinguishable difference from the $R\bar{3}m$ and *C*2/*c* structures, **Figure 4A**. The Sr-substitution results in the addition of a disordered 3-fold Sr site. This Sr site is increasingly occupied with additional Sr substitution, but only one of the four possible positions can be occupied at one time. The $\boldsymbol{A_{ii}}$ layer is ordered in all three structural models, **Figure 4B**. **Figure 4C** illustrates the relationship between the Zn_2As_3 layers of the three structures. The *C*2/*c* structure illustrated an ordered puckered trigonal planar Zn layer resulting from Zn vacancies. The $R\bar{3}m$ and $R\bar{3}$ structures illustrate a similar puckered planar Zn layer where the Zn sites are only 2/3 occupied and the layer isn't perfectly flat which would result in a layer with Zn vacancies that is similar to the puckered trigonal planar layer of the *C*2/*c* structure. The

rare pseudo trigonal-planar geometry of the Zn-As layer is comparable to those found in Sr_2ZnAs_2[19] or the ordered Zn-As layers of KZnAs[31] that lack vacancies and preserve their hexagonal symmetry. The Sn_2As_6 layers are depicted in **Figure 4D**. The structure crystallizing in the *C2/c* space group illustrates an ordered layer of Sn_2As_6, staggered ethane-like, pillars separated by Eu atoms. In the *C2/c* structure this Sn layer was described by a stacking perturbation where the layer was shifted. The $R\bar{3}m$ and $R\bar{3}$ structures better describe this stacking perturbation as substitutional disorder, due to partial occupancies of the atom sites in the layer. In these structures, the Eu3 sites are situated along the Sn-Sn bond; however, both sites cannot be occupied at the same time. The Sn site is occupied 1/3 of the time, and the Eu site is occupied 2/3 of the time. Various anionic motifs have been reported for Sn-As Zintl phases,[32–37] but the isolated Sn_2As_6 ethane-like units of $Eu_{11}Zn_4Sn_2As_{12}$ are most like those of $Sr_{14}Sn_3As_{12}$ and $Eu_{14}Sn_3As_{12}$, although the latter are more distorted with a longer Sn-Sn bond.[18]

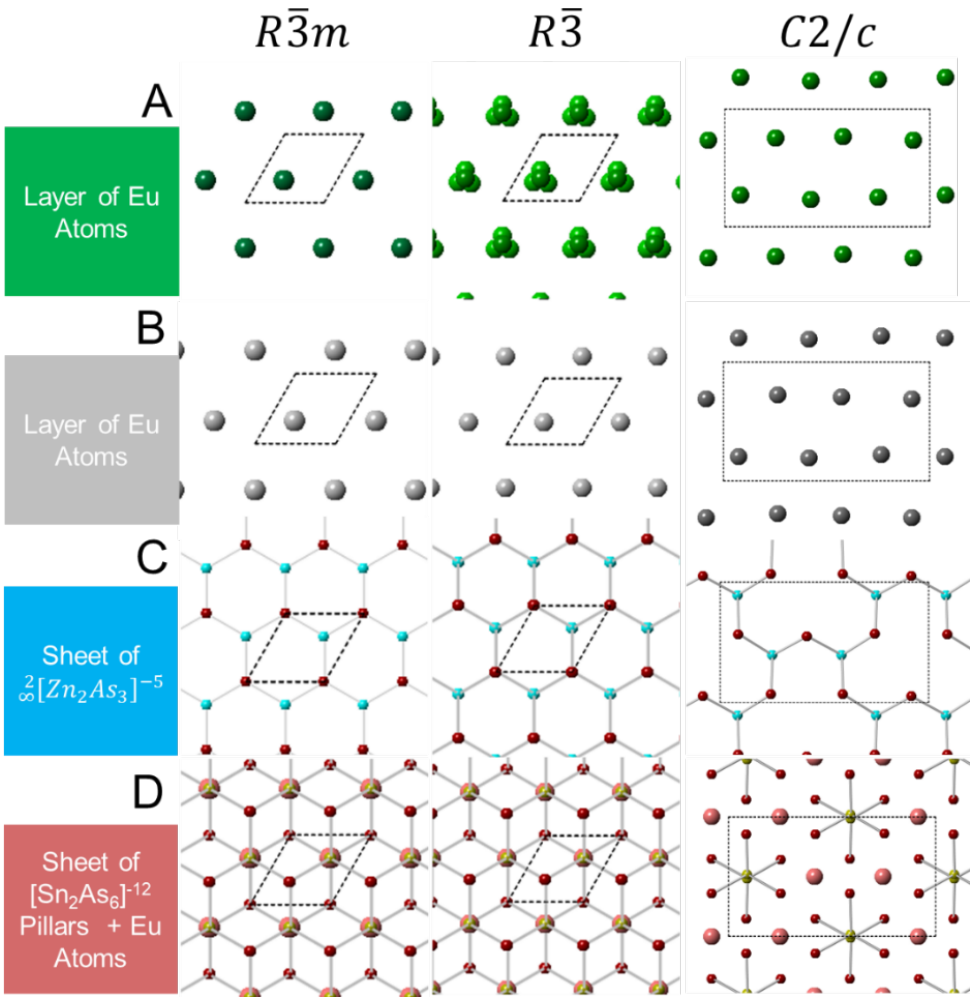

Figure 4. Comparisons of the (A) $\mathbf{A_i}$ Eu layer, (B) $\mathbf{A_{ii}}$ Eu layer, (C) Zn_2As_3 layer, and (D) Sn_2As_6 pillars in the $R\bar{3}m$, $R\bar{3}$, and $C2/c$ space groups, shown in projection down the *c* axis. The occupational vacancies in the Zn, Sn and Eu3 sites in the $R\bar{3}m$ and $R\bar{3}$ structures are not indicated, but the Zn sites are only 2/3 occupied, the Sn site is occupied 1/3 of the time, and the Eu3 site is occupied 2/3 of the time.

As shown in **Figure 5A** for the solid solution $Eu_{11-x}Sr_xZn_4Sn_2As_{12}$, as *x* increases, the occupancy of Sr on the Eu1 and Eu3 sites increases; however, the Eu2 site is best described as having vacancies, and a newly generated Sr site that is described by both vacancies and positional disorder. For the Eu2/Sr2 site, as *x* increases, the occupation of Eu2 decreases, and the Sr2 site occupancy increases. The Eu-Eu interatomic distances increase with the addition of Sr, **Figure 5B**. The Eu1 – Eu1, Eu2 – Eu2, and Eu3 – Eu3 intralayer interatomic distances are determined by the unit cell *a* axes and do not change significantly with *x*. The shortest interatomic distance is between the interlayer Eu1 – Eu2 that are separated by the Zn_2As_6 layer. The three Eu sites are coordinated by six As atoms from either the Zn_2As_6 or Sn_2As_6 layers, and the polyhedral volume of these sites increases with the addition of Sr, **Figure 5C**.

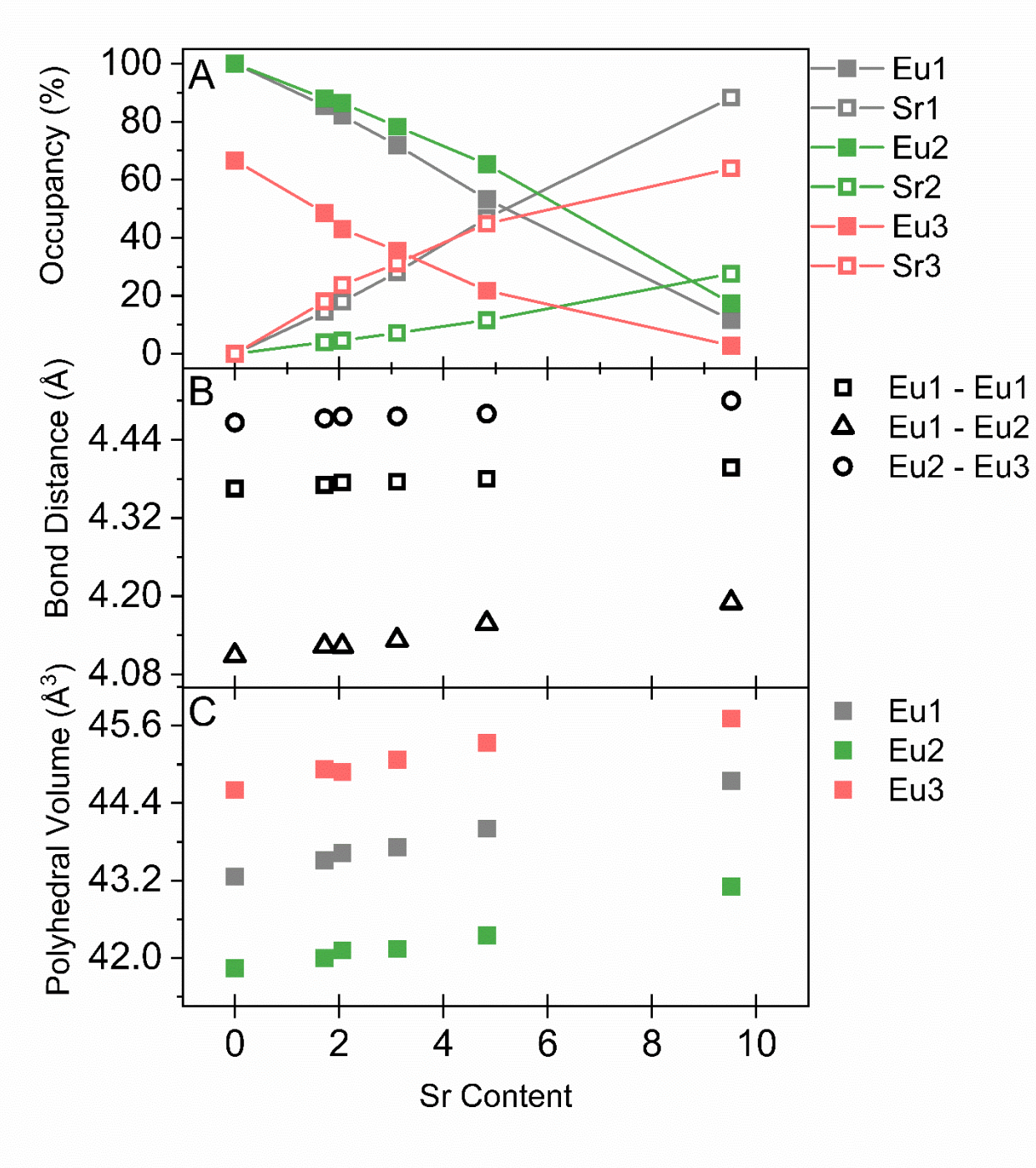

Figure 5. (A) Site occupancy as a function of increasing Sr. The maximum site occupancy for Eu3/Sr3 is ~66% due to the site being 2/3 occupied. (B) Eu – Eu interatomic distances below 8 Å where Eu1 – Eu1 = Eu2 – Eu2 = Eu3 – Eu3 (intralayer) and (C) Eu site polyhedral volume where Eu2 = Sr2.

Polycrystalline Properties

In order to confirm the magnetic properties previously reported,[13] a polycrystalline sintered pellet of $Eu_{11}Zn_4Sn_2As_{12}$ was investigated. The magnetic susceptibility was measured from 2 K to 300 K at 1 T (**Figure 6A**). A portion of the data (35 - 300 K) in the paramagnetic region (1 T) was fit utilizing the Curie-Weiss law, $\chi(T) = C/(T-\theta)$, where χ is the molar susceptibility, C is the Curie constant ($C = N_A\mu_{eff}^2/k_B$), and θ is the Curie-Weiss temperature, yielding an effective moment of 7.754(6) μ_B per Eu atom, which is slightly lower, but in reasonable agreement with the expected theoretical moment. The positive Curie-Weiss temperature of 12.3(2) K indicates ferromagnetic coupling between Eu^{2+} spins, consistent with single crystal data.[13] The magnetization versus field was measured at 2 K from 7 to -7 T (**Figure 6B**). Similar to the single crystal data, the polycrystalline sample showed no coercive field, and only 7 Eu^{2+} align with the field up to ~ 5 T, leaving 4 Eu^{2+} ions antiferromagnetically aligned. Above ~5T, the moment starts to rise again, suggesting that the 4 Eu^{2+} ions will ferromagnetically align with a high enough field. The resulting curve is compared to the curves of a single crystal measured ||*c* and ||*ab*. The polycrystalline magnetization should fall between the ||*ac* and ||*c* curves. The magnetic susceptibility of a single crystal ||*ab* is presented in **Figure S4**. However, the PXRD refinement of the polycrystalline shows that there are small impurities (**Table S4**), which likely account for the deviation. The curve of the polycrystalline sample exhibits a plateau in magnetization that is not as flat as the single crystal measured ||*c*, but in qualitative agreement with the single crystal measured ||*ab*. The resistance as a function of magnetic field was measured on a rectangle cut from the same dense pellet as the initial cube. The peak resistivity is at a slightly higher temperature, 18 K, with a maximum negative CMR of 588-fold, **Figure S5**; for comparison, the resistivity exhibits a 207-fold decrease at 9 T and 14 K. Consistent with a polycrystalline sample with grain boundaries, the resistivity is 10^3 higher than single crystal, but qualitatively, the temperature and field dependence is the same.

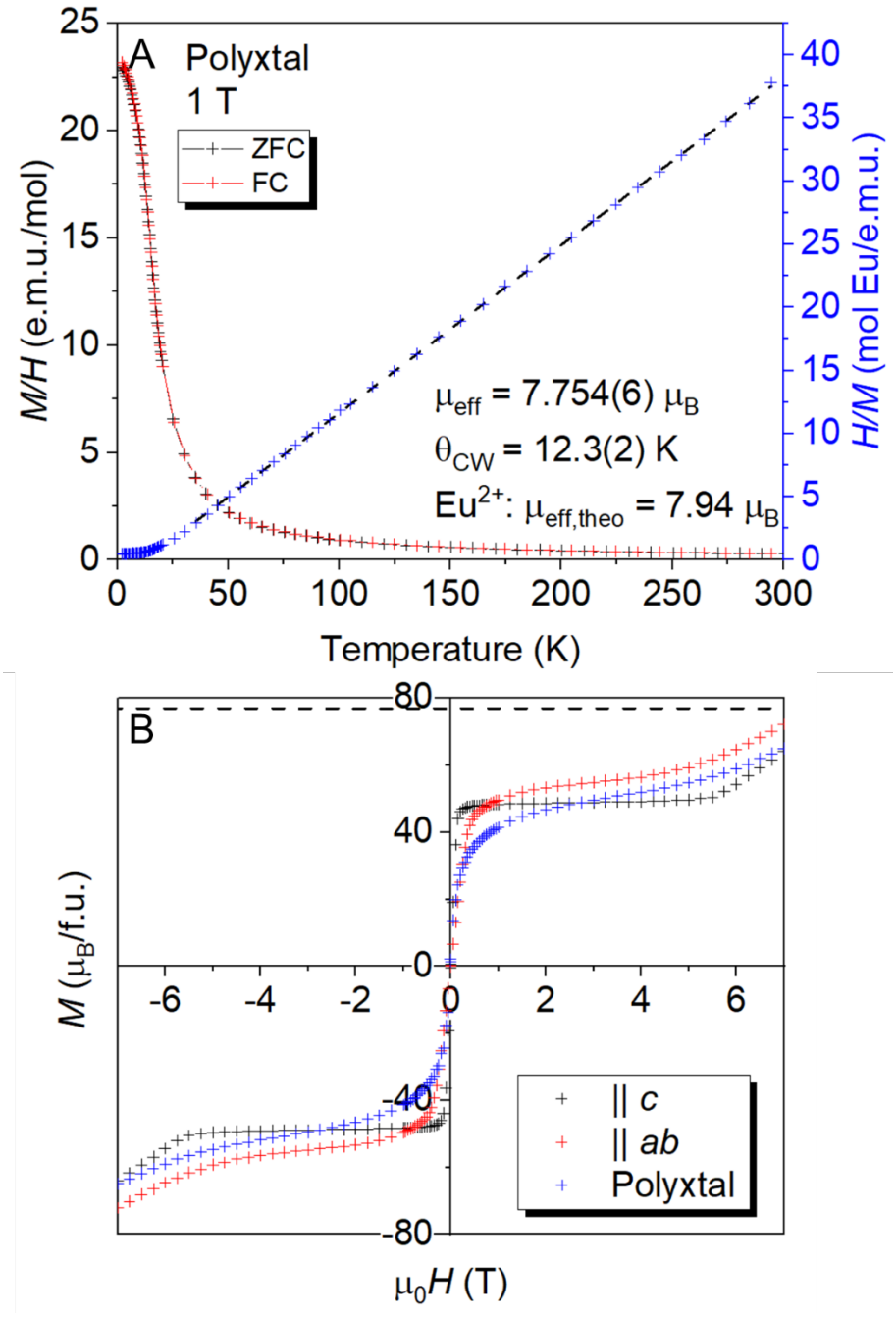

Figure 6. (A) Molar magnetic susceptibility of polycrystalline $Eu_{11}Zn_4Sn_2As_{12}$ in an applied field of H = 1 T, the inverse susceptibility (blue), and its Curie – Weiss fit (black dash) and (B) M vs H curve at T = 2 K of polycrystalline $Eu_{11}Zn_4Sn_2As_{12}$ (blue) compared to the curves of a $Eu_{11}Zn_4Sn_2As_{12}$ single crystal parallel to *c* (black) and parallel to *ab* (red).

Magnetization under higher fields

The AC susceptibility (χ_{AC}) versus field was studied from H = -18 T to H = 18 T for a single crystal of $Eu_{11}Zn_4Sn_2As_{12}$ at T = 2 K, 5 K, 8 K, and 30 K and from H = 0 T to H = 18 T for T = 11 K, **Figure 7A**. Since the ac susceptibility measures the derivative of magnetic moment (χ_{AC} ~ dM/dH), kinks can appear when M(H) changes its slope with varying DC fields. At low temperatures (T = 8 K and below), such features are clearly seen at the corresponding fields observed in **Figure 6B**. Above the transition temperature, the AC susceptibility lacks in such features and mostly shows a parabolic-like background. Exploiting the relation between magnetization and AC susceptibility, we estimate the magnetization (M_{ac}) from the AC susceptibility data by the following procedure. First, the background of the susceptometer is obtained by an empirical fitting (third-order polynomial) of the high field data (H > 9 T), which then is extended to the whole field region (**Figure S6).** The background subtracted data were then integrated as a function of the field, which gave almost field independent values at H = 0.2 - 5 T, where the DC magnetization plateau also occurs. The final result shown in **Figure 7B** was obtained by scaling the flat region to the DC magnetization plateau for T = 2 K. For the measurements done at T = 8 K and T = 11 K, the background fitting becomes subjective; therefore, the analyzed data for T = 2 K and T = 5 K is compared back to the experimental data and used to understand the changes in the data collected at T = 8 K and T = 11 K.

The magnetization at 2 K resembles the DC measurement reported in Devlin et al[13] and above for the polycrystalline sample. The plateau is more well-defined in the AC measurement at T = 2 K, and the final saturation of all 11 Eu^{2+} ion at 77 μ_B occurs at H = ~ 8 T. As the temperature increases this plateau become gentler until it is a smooth slope through the final saturation, **Figure 7A**. The plateau in the magnetization is equivalent to 7 Eu^{2+} ions, leaving 4 Eu^{2+} ions antiferromagnetically coupled. These remaining antiferromagnetically coupled Eu^{2+} ions become ferromagnetically aligned with the applied field at H = ~ 8 T, similar to the DC magnetization data previously published and shown for the polycrystalline sample in **Figure 6**. The crystal was rotated in the field and measured transversely (perpendicular to *c*) and shows little temperature dependence, **Figure S7**. The magnetization is similar to the MPMS transverse measurement, **Figure 6B**, or the T = 8 K and T = 11 K measurements in **Figure 7A**, where the plateau is not as flat as the longitudinal (along *c)* magnetization. The magnetization was taken at T = 30 K, above the T_c, to illustrate the difference between the slope to a full final saturation moment and paramagnetic behavior.

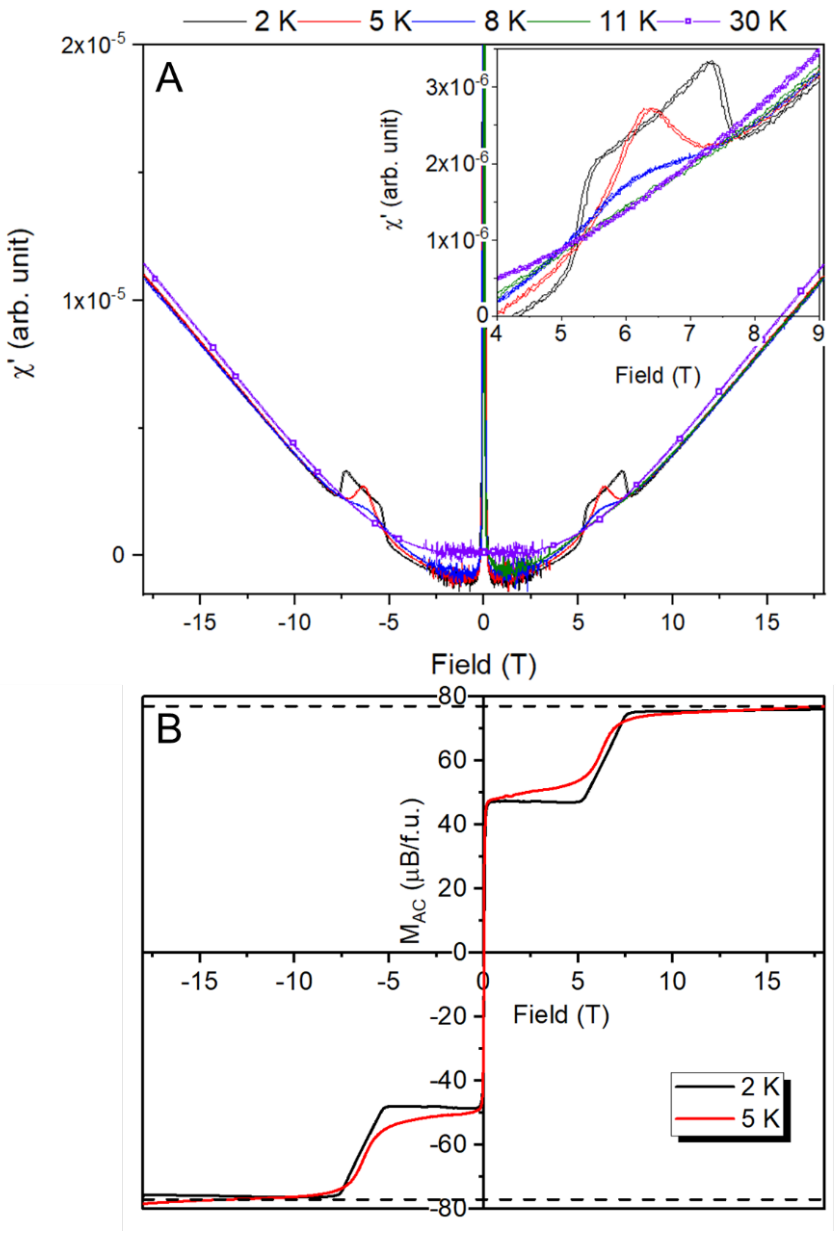

Figure 7. (A) The ac susceptibility vs field of $Eu_{11}Zn_4Sn_2As_{12}$ from H = -18 T to H = 18 T, longitudinally: the inset shows the expanded region between H = 4 T and H = 9 T. The noise at low fields is due to the flux jump of the superconducting magnet. (B) Estimated longitudinal or transverse magnetization (M_{ac}) vs field of $Eu_{11}Zn_4Sn_2As_{12}$ from H = 0 T to H = 18 T at T = 2 K and T = 5K. The magnetization was estimated by integrating background removed ac susceptibility data followed by scaling the result between H = 0.2 and H = 5 T to the flat DC magnetization moment at the same field region (see text).

The temperature dependence of the electrical resistivity was measured longitudinally (along *c)*, **Figure 8A**, and transversely (perpendicular to *c)*, **Figure S8**, across a single crystal at different applied fields. **Figure 8B** illustrates the magnetoresistance (MR), $\frac{|\rho(H)-\rho(0)|}{\rho(H)}$, as a function of temperature. The decrease in resistivity with applied field is calculated via $\frac{\rho(O)}{\rho(H)}$. The previously published CMR behavior exhibited a 2690-fold decrease in resistivity at T = 14 K.[13] This behavior is confirmed in the longitudinal direction down the *c*-axis with a 6321-fold decrease in resistivity at H = 9 T, ~2.3x larger than previously published results, and an 8213-fold decrease in resistivity at H = 18 T. The difference is attributed to differences in carrier concentration of the single crystal samples. The transverse direction showed a 1667-fold decrease in resistivity near the transition temperature at H = 18 T. Additionally, R(H) was measured by sweeping fields at fixed temperatures (T = 2.1, 5, 8, 11, 14, and 30 K), **Figure S9**.

For comparison, $Eu_{11}Zn_4Sn_2As_{12}$ has a 160-fold decrease in resistivity ($\frac{\rho(O)}{\rho(H)}$) with a H = 3 T field at the T = 14 K transition temperature. $Eu_{14}MnSb_{11}$ has an estimated 1.4-fold decrease (T = ~ 92 K) and $EuIn_2As_2$, a layered Zintl phase, exhibits an estimated 2.0-fold decrease (T = ~17 K) in CMR at H = 3 T. While the CMR for $Eu_{11}Zn_4Sn_2As_{12}$ is large compared to these two Zintl phases, it is smaller than the estimated 5556-fold decrease (T = ~ 17 K) in resistivity at H = 3 T of the Zintl phase, $Eu_5In_2As_6$, whose CMR mechanism is attributed to magnetic polarons.[12] One signature for magnetic polarons is a deviation from the Curie-Weiss fit above the Curie temperature.[12] There is little to no deviation from the CW fit for $Eu_{11}Zn_4Sn_2As_{12}$[13] and a small deviation seen in the $\chi T(T)$ plot, **Figure S10.** The $\chi T(T)$ plot shows a ferromagnetic transition at a higher temperature than the Curie Weiss temperature of T = 12.3 K but is consistent with the magnetoresistance onset. Further evidence is necessary to determine if the formation of polarons contribute to the CMR in this example.

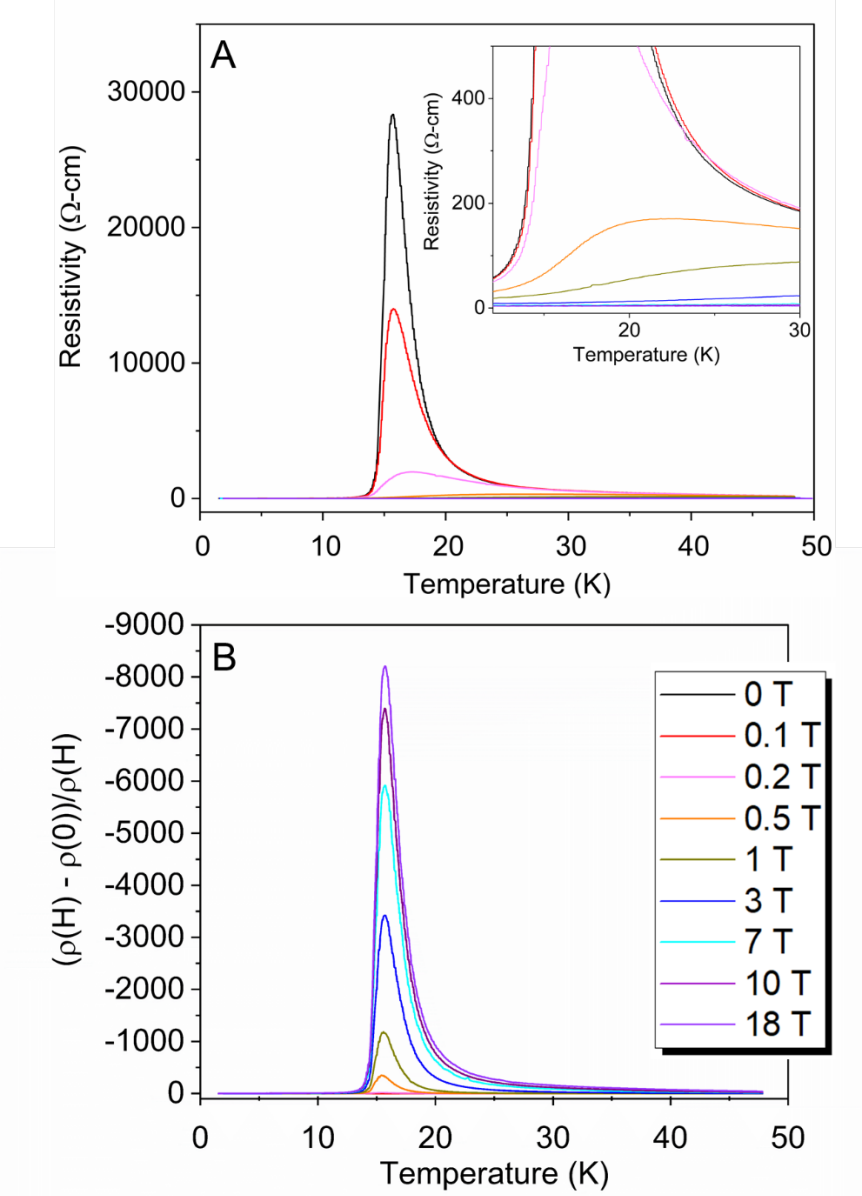

Figure 8. (A) Temperature-dependent electrical resistivity of a $Eu_{11}Zn_4Sn_2As_{12}$ single crystal measured longitudinally (along *c)* at applied magnetic fields of H = 0, 0.1, 0.2, 0.5, 1, 3, 7, 10, and 18 T. The inset shows the temperature-dependent electrical resistivity from T = 12 - 30 K at different applied magnetic fields. (B) Magnetoresistance as a function of temperature at the applied magnetic fields.

$Eu_{11-x}Sr_xZn_4Sn_2As_{12}$ Magnetic Data

In order to identify the 7 ferromagnetic Eu^{2+} ions accounted for by the initial plateau in M v H data and the 4 Eu^{2+} antiferromagnetically aligned ions, the structure was substituted with non-magnetic Sr^{2+}. Single crystals of composition *x* = 2.0, 2.2, 5.5, and 9.4 (**Table 1)** were examined. **Figure**

S11 shows the backscattered image and elemental maps of Eu, Sr, Zn, Sn, and As for these single crystals. The elements are well-dispersed throughout the crystals with small excesses of Sn found on the surface of the *x* = 5.5 and 9.4 crystals.

Table 1. Summary of EMPA Compositions and Compositions used for MPMS Analysis

Loaded Composition	EMPA Composition	MPMS Composition
$Eu_9Sr_2Zn_4Sn_2As_{12}$	$Eu_{9.1(1)}Sr_{2.0(2)}Zn_{3.99(7)}Sn_{1.97(3)}As_{11.95(9)}$	$Eu_9Sr_2Zn_4Sn_2As_{12}$
$Eu_9Sr_2Zn_4Sn_2As_{12}$	$Eu_{8.8(1)}Sr_{2.2(8)}Zn_{4.09(4)}Sn_{1.93(3)}As_{11.97(8)}$	$Eu_{8.8}Sr_{2.2}Zn_4Sn_2As_{12}$
$Eu_5Sr_6Zn_4Sn_2As_{12}$	$Eu_{5.5(1)}Sr_{5.5(2)}Zn_{3.91(3)}Sn_{2.04(1)}As_{12}$	$Eu_{5.5}Sr_{5.5}Zn_4Sn_2As_{12}$
$Eu_2Sr_9Zn_4Sn_2As_{12}$	$Eu_{1.57(2)}Sr_{9.8(1)}Zn_{3.96(8)}Sn_{2.09(3)}As_{12}$	$Eu_{1.6}Sr_{9.4}Zn_4Sn_2As_{12}$

The magnetic susceptibility was measured longitudinally on single crystals from T = 2 K to T = 300 K at H = 3 T, **Figure 9**. At this field, there is no difference in ZFC and FC data. The parent $Eu_{11}Zn_4Sn_2As_{12}$ compound exhibits paramagnetic behavior above T = 15 K, and a fit of this portion (T = 35 K to T = 300 K) of data utilizing the Curie-Weiss law and yields effective moments, μ_{eff}, listed in **Table 2**, which are slightly lower, but in reasonable agreement with the theoretical moment if all the Eu atoms were divalent Eu^{2+} cation (7.94 μ_B). The Curie-Weiss temperature decreases with increasing Sr content and fitting the data for the *x* = 9.4 crystal, results in a negative Curie-Weiss temperature, **Table 2**. The positive Curie-Weiss temperature indicates ferromagnetic coupling between Eu^{2+} spins, consistent with the observed ferromagnetic ordering. The negative Curie-Weiss temperature obtained for the *x* = 9.4 crystal indicates antiferromagnetic coupling between Eu^{2+} spins. Due to the magnetic susceptibility being measured at a high field, the exact T_C cannot be determined; however, the derivative of the χ v T is plotted, **Figure S12**, showing that with increasing Sr content the T_C is shifting to lower temperatures.

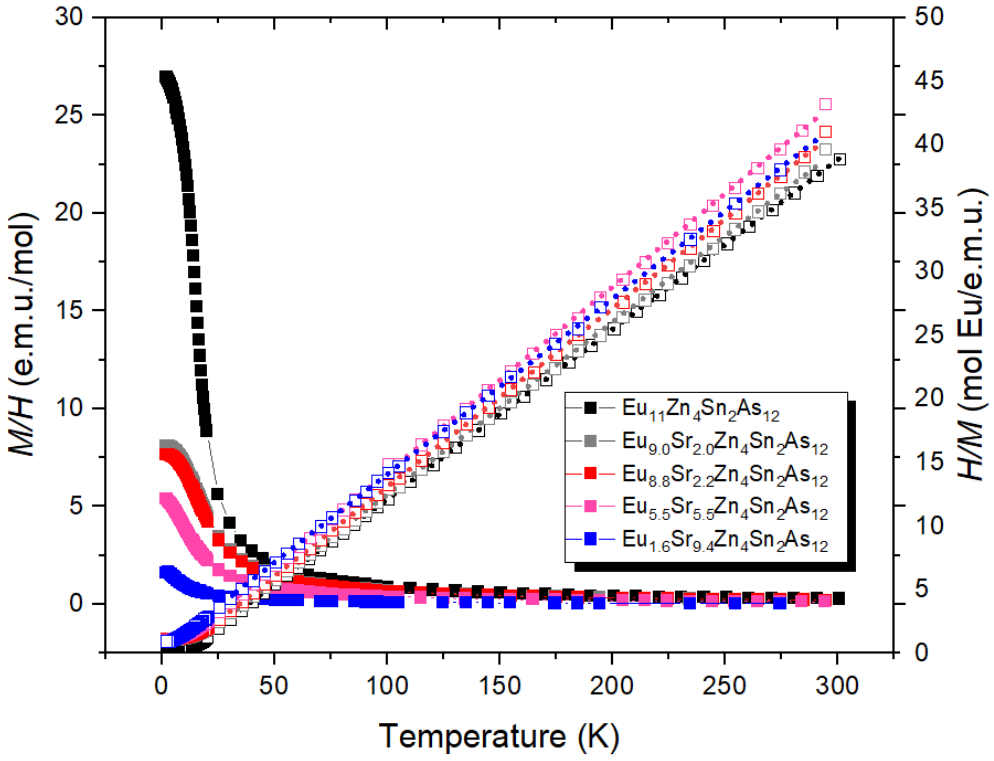

Figure 9. Molar magnetic susceptibility of $Eu_{11-x}Sr_xZn_4Sn_2As_{12}$ (x = 2.0, 2.2, 5.5, and 9.4) in the applied filed of H = 3 T (closed squares), inverse susceptibility as open squares and the Curie-Weiss fits (dotted lines). The data are compared to the parent compound $Eu_{11}Zn_4Sn_2As_{12}$ taken at H = 1 T.[13]

Table 2. Results from Curie-Weiss fit of $Eu_{11-x}Sr_xZn_4Sn_2As_{12}$ (x = 2.0, 2.2, 5.5, and 9.4).

Eu Content	C	θ_{CW}	μ_{eff}*
11‡		9.2(1)	7.74(1)
9.0	7.38(2)	7.8(4)	7.68(1)
8.8	7.12(1)	6.8(3)	7.54(1)
5.5	6.82(2)	3.2(4)	7.39(1)
1.6	7.24(1)	-1.8(2)	7.61(1)

*μ_{eff} = sqrt(7.99C)

‡ From Devlin et al.[13]

Magnetization versus field was measured longitudinally at T = 2 K for single crystals of $Eu_{11-x}Sr_xZn_4Sn_2As_{12}$ (x = 2.0, 2.2, 5.5, and 9.4) from H = -7 T to H = 7 T are compared with $Eu_{11}Zn_4Sn_2As_{12}$, **Figure 10A**. The plateau in the parent compound is attributed to 7 ferromagnetically and 4 antiferromagnetic Eu^{2+} ions, and the higher field plateau is the ferromagnetic saturation of all 11 Eu^{2+} ions. At low Sr concentrations, x = 2.0 and 2.2, the

magnetization experiences a slower increase in the first plateau at lower fields and a sharper slope towards the full saturation after H = 5 T, but neither crystal reaches full saturation (~63 μ_B for 9 Eu^{2+} ions). The loss of the distinct transition to higher magnetization upon Sr incorporation may indicate that the Eu sites that are substituted with Sr first are likely the antiferromagnetically aligned Eu^{2+} ions in the parent compound.

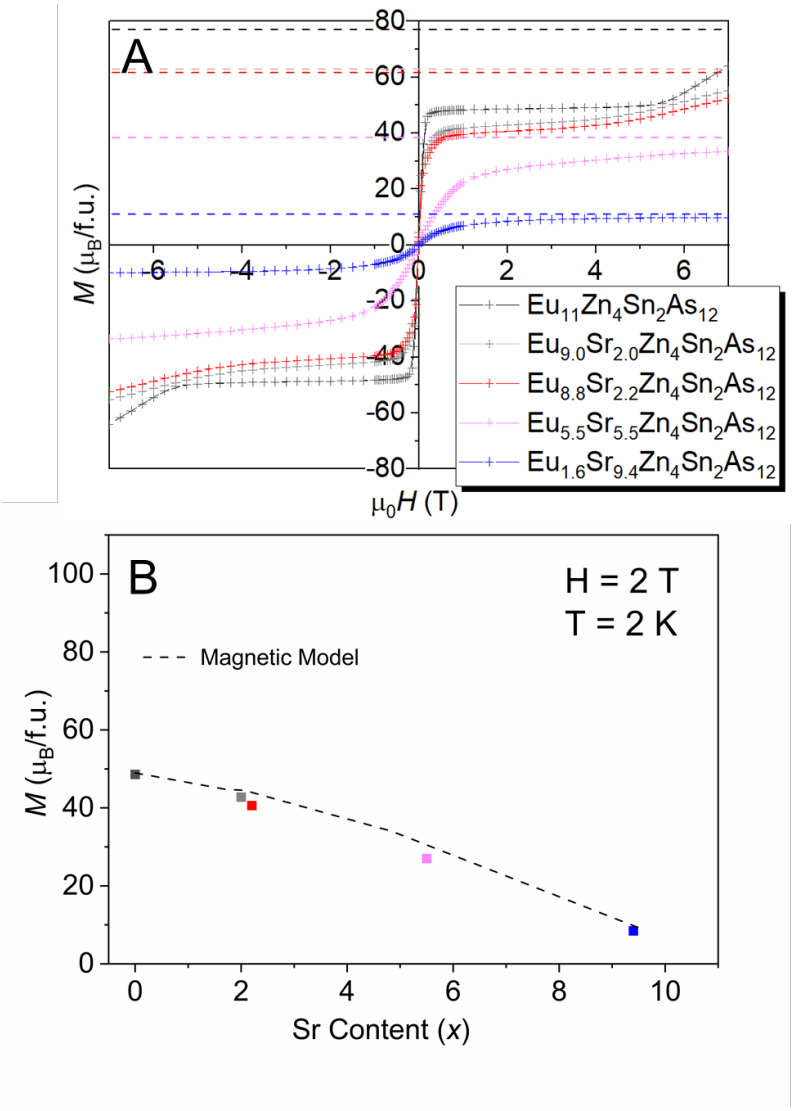

Figure 10. (A) M v H curves at 2 K of $Eu_{11-x}Sr_xZn_4Sn_2As_{12}$ (x = 2.0, 2.2, 5.5, and 9.4) compared to the parent compound $Eu_{11}Zn_4Sn_2As_{12}$ where the dashed lines indicate the corresponding saturation moment for each compound.[13] (B) The magnetization of each sample at H = 2 T and T = 2 K as a function of Sr composition, x, along with the calculated magnetic moment based on

the model (see **Figure S13**) utilizing the occupancies of the Eu1, Eu2, and Eu3 from single crystal refinements.

The non-trivial nature of the Eu-Eu interactions is illustrated by the decrease in magnetization of the M(H) measurement; the x = 2.2 measurement will be used as an example. At H = 2 T, the central field of the plateau, the magnetization is reduced from 48.2 μ_B/f.u. (x = 0) to 40.5 μ_B/f.u. (x = 2.2). This decrease in magnetization corresponds to ~ 1.1 Eu^{2+} ions; however, the total Sr from EMPA is x = 2.2, double the amount corresponding to the observed decrease in magnetization. Additionally, none of the individual Eu sites have decreased by 1.1 for the corresponding single crystal sample, **Figure 5**, (x = 2.06). The Eu1, Eu2, and Eu3 sites are occupied by 0.539, 0.813, and 0.710 Sr atoms (per f.u.), respectively. For the magnetization data of the x = 5.5 and x = 9.4 single crystals, the high field saturation plateau is eliminated. In the x = 5.5 crystal, the magnetization has not reached saturation at 7 T; at low field, the moment is ~25 μ_B (~4 Eu^{2+}), and at high field, the moment is ~35 μ_B (~5 Eu^{2+}), close to that expected for all remaining Eu^{2+} ions. However, the x = 9.9 crystal appears to be fully saturated at ~ 5 T with a moment of ~10 μ_B, consistent with a composition of x closer to 9.6 and 1.4 Eu^{2+} ions.

The analysis of the structure of $Eu_{11-x}Sr_xZn_4Sn_2As_{12}$ may give insight to which Eu-Eu interactions result in the two different plateaus, < 1 T and ~ 8 T. The decreasing plateau below 8 T with respect to temperature in the longitudinal direction and the non-temperature dependent nature of the transverse M(H) ac measurements, **Figures 7** and **S6**, might imply that the Eu^{2+} ions responsible for the plateau in magnetization are likely within the same layer, as opposed to two layers interacting. The intralayer distances between Eu atoms are found for Eu1 – Eu1, Eu2 – Eu2, and Eu3 – Eu3 to be equivalent (4.3652(9) Å, x = 0) in the structures, and each of these interactions alone could not result in the plateau at 49 μ_B/f.u corresponding to 7 Eu atoms due to the previously described multiplicities. Alternatively, the interlayer Eu1 – Eu2 distance is the shortest in the structure (4.1085(10) Å, x = 0) and may provide a possible antiferromagnetic interaction. However, the Eu1 site accounts for 3 equivalent sites, and Eu2 accounts for 6 equivalent sites and therefore cannot account for the plateau at 49 μ_B/f.u. A simple structural analysis based on interatomic distance to account for a strong antiferromagnetic coupling does not exist if we assume full occupancy of the various sites. However, an alternative structural model can be envisioned to account for the antiferromagnetic coupling. As previously mentioned, the Eu1 and Eu2 sites accounts for 3 and 6 Eu^{2+} ions in the structure, and the Eu3 site accounts for 2. Assuming that all Eu sites are ferromagnetically aligned (intralayer) and the Eu3 site, which is

partially occupied (2/3), is antiferromagnetically aligned with respect to the Eu1 and Eu2 sites (interlayer), reasonable agreement to the magnetic data is possible (**Figure 10B**). This model, illustrated in **Figure S13**, results in the correct ferromagnetic and antiferromagnetic interactions for the initial magnetic saturation plateau. The antiferromagnetic coupling between partially occupied Eu3 and the Eu2 sites, through the As layers from the Sn_2As_3 pillars, leads to interlayer interactions equivalent to a total 2 antiferromagnetic (4 atoms) with 1 ferromagnetic, with the rest of the atoms ferromagnetic (6). Therefore, the interlayer coupling gives rise to a total of 7 ferromagnetic and 4 antiferromagnetically coupled Eu^{2+}. This model agrees well with the nontrivial nature of the changes in magnetic moment and the reduction of moment and loss of antiferromagnetic coupling as Sr is introduced in the Eu2 layer, as can be seen from the agreement between the calculations based on this model and the data, **Figure 10B**.

^{151}Eu and ^{119}Sn Mössbauer Spectroscopy

^{151}Eu and ^{119}Sn Mössbauer spectroscopies were carried out to determine the Eu and Sn valence states and to investigate the Eu sublattice. Samples made from ground single crystals of compositions $Eu_{11-x}Sr_xZn_4Sn_2As_{12}$ (x = 0, 1, and 2; denoted Eu_{11}, $Eu_{10}Sr$, and Eu_9Sr_2) and a sample made from $Eu_{11}Zn_4Sn_2As_{12}$ synthesized using metallurgical methods (denoted Eu_{11}*) were investigated between 295 and 7 K.

The T = 295 K spectra in **Figure 11** reveal the isomer shift for $Eu_{11-x}Sr_xZn_4Sn_2As_{12}$ (x = 0, 1, and 2) for both ^{151}Eu and ^{119}Sn. The solid line in each spectrum corresponds to a fit with Eu(II) centered at about -11.0(2) mm/s for all samples, and a Eu(III) impurity corresponding to ~5% of the spectral area with an isomer shift of 0.7(1) mm/s, characteristic for Eu(III), **Figure 11A**. The isomer shift is typical of covalent Eu(II) and is similar to those reported for other Eu-containing phases such as $Eu_{14}MnAs_{11}$ (-10.66(5) mm/s),[38] $Eu_{14}MnSb_{11}$ (-10.80(3) mm/s),[38] and EuZnSn (-10.88(3) mm/s,[39] and other intermetallic europium arsenides, such as $EuAg_4As_2$,[40,41] $Eu_5In_2As_6$,[42] Eu_3AlAs_3, [42] and Eu_3GaAs_3.[42] The $Eu_{11-x}Sr_xZn_4Sn_2As_{12}$ solid-solution has three crystallographically unique Eu sites, which are not distinguished by room-temperature Mössbauer spectroscopy, and one crystallographically unique Sn site. The T = 295 K spectra in **Figure 11B** reveal an isomer shift of ^{119}Sn from 1.75(1) mm/s for the samples and a quadrupole splitting of ~0.5 mm/s. The isomer shift is intermediate between Sn(II) and Sn(IV) and similar to that of intermetallic Sn, such as observed in α-Sn,[43] Mg_2Sn,[43] or Pt-Sn alloys.[44] As there is no known reference for Sn(III), we can

only establish that Sn is neither di- nor tetravalent and in the intermetallic range. The isomer shift and quadrupole splitting for ^{151}Eu and ^{119}Sn at T = 295 K are listed in **Table 3**.

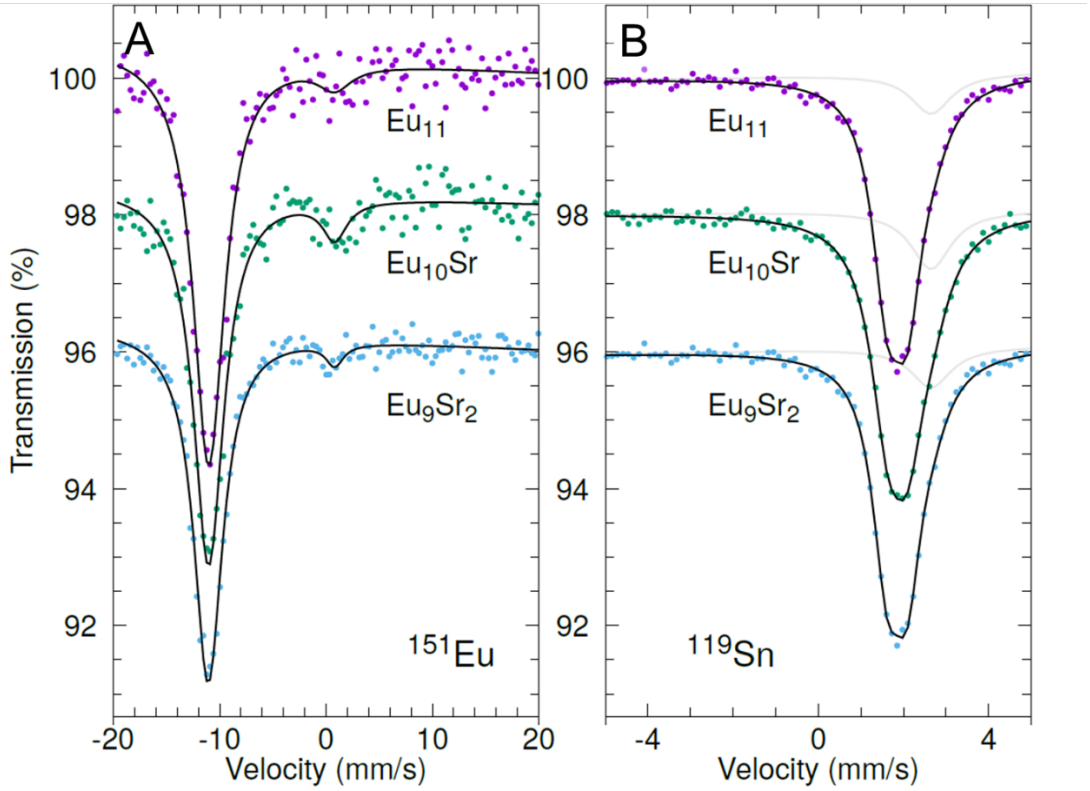

Figure 11. (A) ^{151}Eu and (B) ^{119}Sn Mössbauer spectra of $Eu_{11-x}Sr_xZn_4Sn_2As_{12}$ (x = 0, 1, and 2) obtained at T = 295 K where the solid line is the result of one Eu(II) component and one Eu(III) impurity component. For ^{119}Sn, the β-Sn component (light gray) was fixed according to parameters obtained from the temperature dependent measurements.

Table 3. ^{151}Eu and ^{119}Sn Spectral Parameters at 295 K and 7 K for $Eu_{11-x}Sr_xZn_4Sn_2As_{12}$ (x = 0, 1, and 2). Hyperfine fields are reported in Figures 13 and S15.

Composition	^{151}Eu		^{119}Sn	
295 K	Isomer Shift δ (mm/s)	% Eu(III)	Isomer Shift δ (mm/s)	Quadrupole Interaction ΔE_Q (mm/s)
$Eu_{11}Zn_4Sn_2As_{12}$	-11.0(1)	<5	1.76(1)	0.56(1)
$Eu_{11}^*Zn_4Sn_2As_{12}$	-11.0(1)	25(2)	1.76(1)	0.56(1)
$Eu_{10}SrZn_4Sn_2As_{12}$	-11.0(1)	9	1.74(1)	0.52(1)
$Eu_9Sr_2Zn_4Sn_2As_{12}$	-11.1(1)	<5	1.74(2)	0.49(1)

7 K	^{151}Eu		^{119}Sn	
$Eu_{11}Zn_4Sn_2As_{12}$	-11.0(2)	13(2)	1.82(1)	-0.24(1)
$Eu_{11}^{*}Zn_4Sn_2As_{12}$	-11.0(2)	3(1)	1.83(1)	-0.24(1)
$Eu_{10}SrZn_4Sn_2As_{12}$	-11.0(2)	12(2)	1.81(1)	-0.21(2)
$Eu_9Sr_2Zn_4Sn_2As_{12}$	-11.0(2)	7(1)	1.81(2)	-0.22(3)

The ^{151}Eu Mössbauer spectra at T = 7 K are provided in **Figure 12**, showing a model with three subsites for Eu(II) (blue) and the Eu(III) impurity site giving the combined fit (black). The isomer shift for the Eu(III) impurity is 0.7(1) mm/s. The spectral area of the Eu(II) exhibits an important increase upon magnetic ordering, indicative of some form of magnetoelastic coupling at low temperatures that leads to a decrease in atomic displacements below the magnetic transition (T = 15 K), **Figure S14**. The magnetoelastic coupling is a possible mechanism for the CMR effect observed in this compound and has been observed in other CMR materials.[45,46] There is no evidence in the spectra for a quadrupole splitting at the Eu sites and this parameter was fixed at zero value. The hyperfine field for Eu is well reproduced by the expected spontaneous magnetization for a spin 7/2. The hyperfine field of ~22 T at 7 K (24.5 T extrapolated saturation value) is typical for divalent europium, and in the range for arsenide e.g., similar to $Eu_{14}MnAs_{11}$,[38] slightly larger than in $Eu_5In_2As_6$,[42] Eu_3AlAs_3,[42] and Eu_3GaAs_3,[42] and somewhat smaller than in $EuAg_4As_2$ [40,41]. Though at least three magnetic components are needed to obtain a good fit, the individual values likely do not convey any specific insights, and the weighted average is displayed in **Figure 13** and used for the isomer shift in **Table 3**. There are only minor differences between the $Eu_{11}Zn_4Sn_2As_{12}$ samples made by single crystal and metallurgical methods; however, the $Eu_{10}SrZn_4Sn_2As_{12}$ and $Eu_9Sr_2Zn_4Sn_2As_{12}$ samples exhibit a lower Curie temperature, as also shown by the magnetometry data in **Figure S12**.

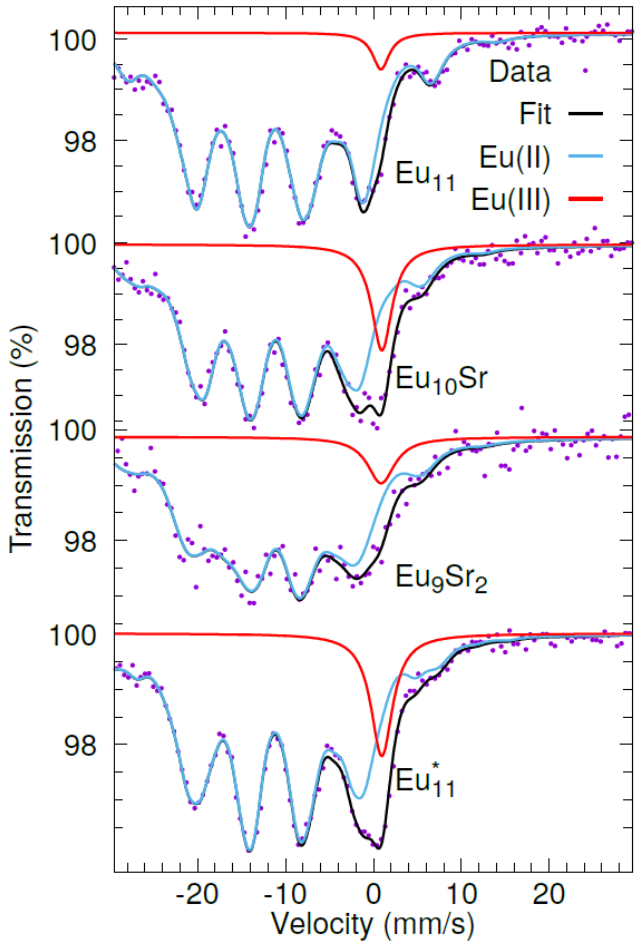

Figure 12. ^{151}Eu Mössbauer spectra of $Eu_{11-x}Sr_xZn_4Sn_2As_{12}$ (x = 0, 1, and 2) and polycrystalline $Eu_{11}Zn_4Sn_2As_{12}$, denoted by Eu*, obtained at T = 7 K where the solid line (black) is the result of three Eu(II) subsites (blue) and one Eu(III) impurity site (red).

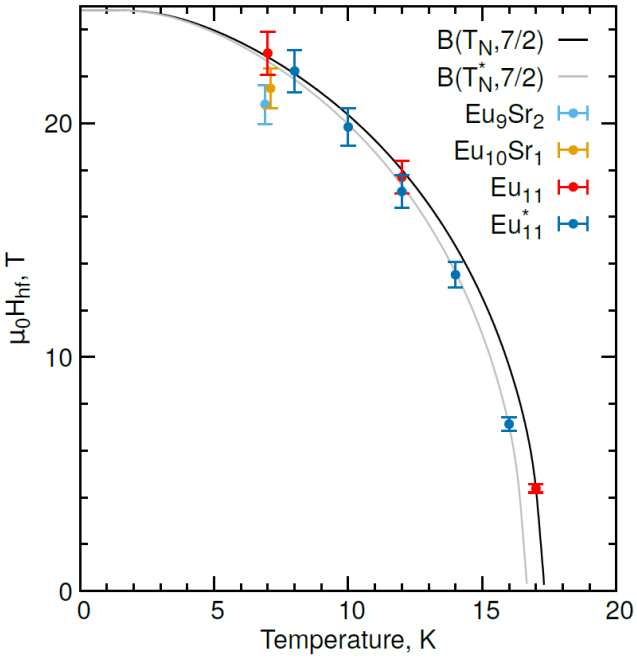

Figure 13. ^{151}Eu temperature dependence of the hyperfine field of $Eu_{11-x}Sr_xZn_4Sn_2As_{12}$ (x = 0, 1, and 2) and polycrystalline $Eu_{11}Zn_4Sn_2As_{12}$, denoted by Eu*.

The magnetically split spectra are more complex for ^{119}Sn than for ^{151}Eu, **Figure S15**. Note that tin does not develop its own magnetic moment and that the magnetic hyperfine splitting occurs from a field transferred by europium neighbors. In addition to a β-Sn flux component,[43] with an observed isomer shift of ~2.55(2) mm/s at 7 K (this β-Sn component is not resolved at 295 K both because of the small area and overlap with the main phase), the fit requires two components with a large hyperfine field parallel and with a small hyperfine field perpendicular to the principle axis of the electric field gradient V_{zz} (i.e. along the Sn-Sn bond), respectively, **Figure 14**. The isomer shift and quadrupole splitting of the two magnetic sub-sites could be constrained for the materials with different Sr content without affecting the quality of the fits. The two components are likely a result of the fractional occupancy of the atoms in the Sn_2As_6 layer resulting in some of the Sn experiencing a different transferred field from the neighboring Eu^{2+} ions and the β-Sn impurity is likely from remaining Sn-flux adhered to the surface of the crystals during sample preparation. The $Eu_{10}Sr_1$, Eu_9Sr_2, and Eu_{11}* materials exhibit broader spectral components that the Eu_{11} material. The latter also exhibits the smallest amount of the small perpendicular field component, which likely originates from site disorder on the Sn or Eu sublattice. Note that the field decreases more rapidly upon heating towards T_C for the site with hyperfine field perpendicular to V_{zz}, which

is another indication of the more disordered nature of this sub-site. The ^{119}Sn spectra also indicates the magnetostriction upon magnetic ordering, as observed in the ^{151}Eu spectra. The lattice parameters of the solid solution were collected only above T = 100 K. If magnetostriction occurs, an anomaly in lattice constants should be observed at ~15 K in future experiments. The ^{119}Sn spectral area analysis for $Eu_{11-x}Sr_xZn_4Sn_2As_{12}$ (x = 0, 1, and 2) and polycrystalline $Eu_{11}Zn_4Sn_2As_{12}$ indicates the presence of a significant amount of β-Sn flux in the samples grown as crystals, whereas the sample grown from metallurgical methods does not exhibit this impurity; a sizeable trivalent europium impurity is however visible in europium-151 spectroscopy. The β-Sn contribution exhibits a characteristically lower Debye temperature than the $Eu_{11-x}Sr_xZn_4Sn_2As_{12}$ phase, **Figure 15**. The different Debye temperatures allow for clean separation of the temperature dependence of the spectra. One single-crystalline sample, $Eu_{10}Sr_1Zn_4Sn_2As_{12}$, has a magnetic impurity that orders at a higher temperature and is likely $Eu_5Sn_2As_6$ which orders ferromagnetically at T = 30 K.[10] A small amount of residual hyperfine splitting is also seen in the Eu_{11}* sample where ~10% $Eu_5Sn_2As_6$ is present in the Rietveld refinement, **Table S4**.

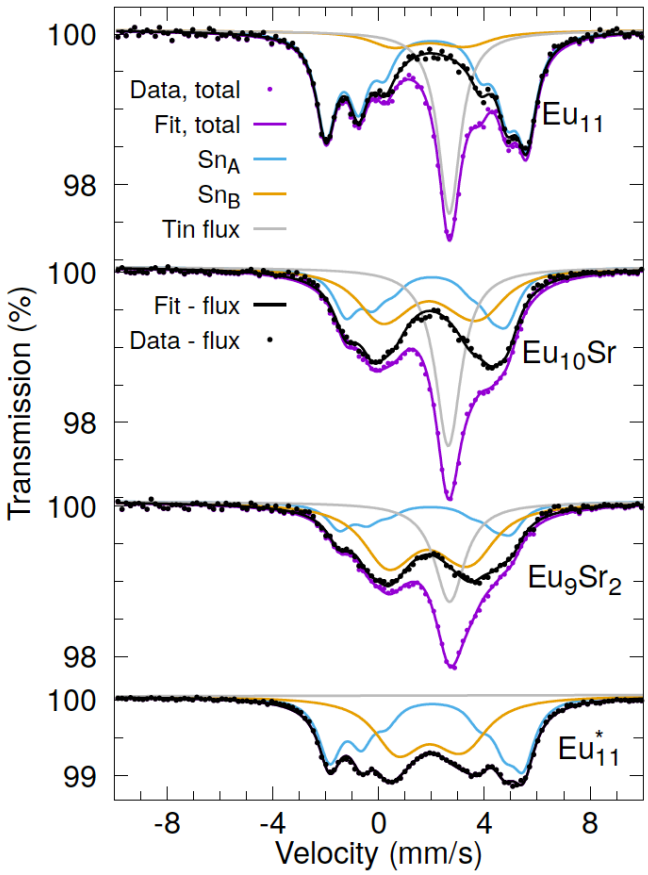

Figure 14. ^{119}Sn Mössbauer spectra at 7 K for $Eu_{11-x}Sr_xZn_4Sn_2As_{12}$ (x = 0,1,2) and polycrystalline $Eu_{11}Zn_4Sn_2As_{12}$ denoted by Eu_{11}*. Sn_A and Sn_B correspond to a large, H = 5 - 7 T, parallel and small, H = 2 - 3 T, perpendicular hyperfine field relative to V_{zz}.

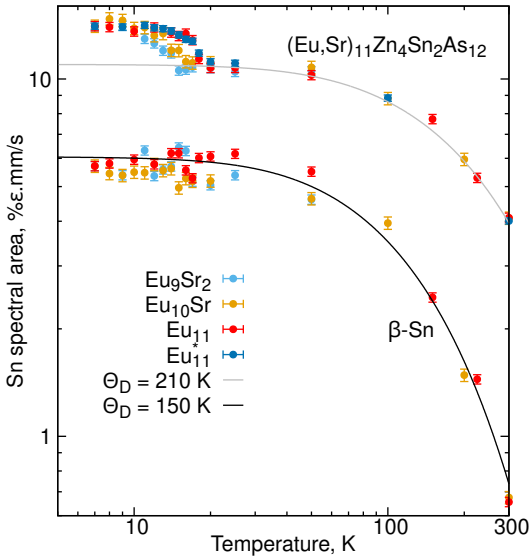

Figure 15. ^{119}Sn spectral area for $Eu_{11-x}Sr_xZn_4Sn_2As_{12}$ (x = 2.0, 2.2, 5.5, and 9.4) and polycrystalline $Eu_{11}Zn_4Sn_2As_{12}$ denoted by Eu*. The β-Sn flux signal and Sn from the Sn_2As_6 ethane-like pillars are indicated by the Debye temperatures of T = 150 K and T = 210 K, respectively. Note the increase in area at the magnetic transition temperature.

Summary.

A new modulated structural model for $Eu_{11}Zn_4Sn_2As_{12}$ is determined to be a trigonal $R\bar{3}m$ structure and the modulated structure for the solid solution $Eu_{11-x}Sr_xZn_4Sn_2As_{12}$ (x < 10) is determined to be a trigonal $R\bar{3}$ structure. The structures exhibit partially occupied Zn_2As_3 puckered layers and sheets of Sn_2As_6 ethane-like species. The magnetization at T = 2 K for the $Eu_{11}Zn_4Sn_2As_{12}$ exhibits a plateau in the magnetization consistent with 7 Eu^{2+} ions below H = 5 T, and the full magnetization of 11 Eu^{2+} ions saturate at H = ~ 8 T. The structural complexity of the solid-solution is elucidated by the change in magnetization of the compound as a function of Sr addition in the solid-solution $Eu_{11-x}Sr_xZn_4Sn_2As_{12}$. A possible model that accounts for the magnetization data is presented. The temperature-dependent ^{151}Eu Mössbauer spectra exhibit an ~ -11.0 mm/s isomer shift for each measured composition, confirming that the Eu atoms in the structure are all Eu^{2+}. The ^{119}Sn exhibits an isomer shift of ~1.8 mm/s for each measured composition, consistent with

a reduced intermetallic-like oxidation state. The Sn shows magnetic hyperfine splitting due to a field transferred from the neighboring Eu^{2+} and the Eu^{2+} magnetic ordering. Both ^{151}Eu and ^{119}Sn Mössbauer spectra show spectral area increase upon magnetic ordering, suggestive of magnetoelastic effects likely associated with either an increase in elastic constant or a decrease in the atomic displacement parameters. The CMR could be induced by either magnetic polarons or magnetoelastic couplings, but both proposed mechanisms require further investigation with low-temperature heat capacity and temperature-dependent structure investigation to confirm.

Acknowledgements

The authors thank Nick Botto for assistance with microprobe analysis, Vaclav Petricek, Michael Dusek, and Oliver Janka for discussions on modulated structures, and Michael Ruf for his help with determining the modulation in one of the compounds using the Bruker APEX3 software. This work was supported by NSF DMR-1709382, DMR-201156-0. Ashlee Hauble acknowledges a UC Davis Dean's Distinguished Graduate Fellowship. A portion of this work was performed at the National High Magnetic Field Laboratory, which is supported by the National Science Foundation Cooperative Agreement No. DMR-1644779 and the state of Florida. The Mössbauer spectral work at Oak Ridge National Laboratory (JZ, RPH) was supported by the US Department of Energy, Office of Science, Office of Basic Energy Sciences, Materials Sciences and Engineering Division.

Supporting Information

Tables of crystal data, structure refinement, atomic coordinates for $Eu_{11-x}Sr_xZn_4Sn_2As_{12}$ ($x < 10$), Table of EMPA compositions compared to single crystal compositions and EMPA elemental mapping, TG/DSC plot of $Eu_{11}Zn_4Sn_2As_{12}$, Rietveld refinement plot and table of refinement statistics, Plots of the CMR of polycrystalline $Eu_{11}Zn_4Sn_2As_{12}$, the transverse measurement of a single crystal, and the R(H) temperature-dependent measurements, Plots of AC susceptibility vs Field background fitting and the ||*ab* AC susceptibility at high fields, χT(T) plots for the investigation of magnetic polarons, Derivative of χ *vs.* T for $Eu_{11-x}Sr_xZn_4Sn_2As_{12}$, Magnetic model for $Eu_{11}Zn_4Sn_2As_{12}$, Eu(II) Mössbauer spectral area and ^{119}Sn temperature dependence of the hyperfine field.

References:

(1) Chan, J. Y.; Kauzlarich, S. M.; Klavins, P.; Shelton, R. N.; Webb, D. J. Colossal Negative

Magnetoresistance in an Antiferromagnet. *Phys. Rev. B* **1998**, *57* (14), 8103–8106.

(2) Wang, J.; Xia, S. Q.; Tao, X. T.; Schäfer, M. C.; Bobev, S. New Ternary Phosphides and Arsenides. Syntheses, Crystal Structures, Physical Properties of Eu_2ZnP_2, $Eu_2Zn_2P_3$ and $Eu_2Cd_2As_3$. *J. Solid State Chem.* **2013**, *205*, 116–121.

(3) Kazem, N.; Kauzlarich, S. M. Thermoelectric Properties of Zintl Antimonides. *Handb. Phys. Chem. Rare Earths* **2016**, *50*, 177–208.

(4) Möchel, A.; Sergueev, I.; Wille, H. C.; Juranyi, F.; Schober, H.; Schweika, W.; Brown, S. R.; Kauzlarich, S. M.; Hermann, R. P. Lattice Dynamics in the Thermoelectric Zintl Compound $Yb_{14}MnSb_{11}$. *Phys. Rev. B - Condens. Matter Mater. Phys.* **2011**, *84* (18), 1–10.

(5) Stoyko, S. S.; Khatun, M.; Mar, A. Ternary Arsenides $A_2Zn_2As_3$ (A = Sr, Eu) and Their Stuffed Derivatives $A_2Ag_2ZnAs_3$. *Inorg. Chem.* **2012**, *51* (4), 2621–2628.

(6) Chanakian, S.; Uhl, D.; Neff, D.; Drymiotis, F.; Park, J.; Petkov, V.; Zevalkink, A.; Bux, S. Exceptionally High Electronic Mobility in Defect-Rich $Eu_2ZnSb_{2-x}Bi_x$ Alloys. *J. Mater. Chem. A* **2020**, *8* (12), 6004–6012.

(7) Chen, C.; Xue, W.; Li, S.; Zhang, Z.; Li, X.; Wang, X.; Liu, Y.; Sui, J.; Liu, X.; Cao, F.; et al. Zintl-Phase Eu_2ZnSb_2 : A Promising Thermoelectric Material with Ultralow Thermal Conductivity. *Proc. Natl. Acad. Sci. U. S. A.* **2019**, *116* (8), 2831–2836.

(8) Zhang, H.; Zhao, J.-T.; Grin, Y.; Wang, X.-J.; Tang, M.-B.; Man, Z.-Y.; Chen, H.-H.; Yang, X.-X. A New Type of Thermoelectric Material, $EuZn_2Sb_2$. *J. Chem. Phys.* **2008**, *129* (16), 164713.

(9) Payne, A. C.; Olmstead, M. M.; Kauzlarich, S. M.; Webb, D. J.; Sprauve, A. E.; Holm, A. P.; Olmstead, M. M.; Kauzlarich, S. M.; Klavins, P. Structure, Magnetism, and Magnetoresistance of the Compounds $Eu_{14}MnAs_{11}$ and $Eu_{14}MnP_{11}$. *Chem. Mater.* **2001**, *13* (4), 1398–1406.

(10) Wang, J.; Xia, S. Q.; Tao, X. T. $A_5Sn_2As_6$ (A = Sr, Eu). Synthesis, Crystal and Electronic Structure, and Thermoelectric Properties. *Inorg. Chem.* **2012**, *51* (10), 5771–5778.

(11) Goforth, A. M.; Klavins, P.; Fettinger, J. C.; Kauzlarich, S. M. Magnetic Properties and Negative Colossal Magnetoresistance of the Rare Earth Zintl Phase $EuIn_2As_2$. *Inorg. Chem.* **2008**, *47* (23), 11048–11056.

(12) Rosa, P.; Xu, Y.; Rahn, M.; Souza, J.; Kushwaha, S.; Veiga, L.; Bombardi, A.; Thomas, S.; Janoschek, M.; Bauer, E.; et al. Colossal Magnetoresistance in a Nonsymmorphic Antiferromagnetic Insulator. *npj Quantum Mater.* **2020**, *52*, 1–6.

(13) Devlin, K. P.; Kazem, N.; Zaikina, J. V.; Cooley, J. A.; Badger, J. R.; Fettinger, J. C.;

Taufour, V.; Kauzlarich, S. M. $Eu_{11}Zn_4Sn_2As_{12}$: A Ferromagnetic Zintl Semiconductor with a Layered Structure Featuring Extended Zn_4As_6 Sheets and Ethane-like Sn_2As_6 Units. *Chem. Mater.* **2018**, *30* (20), 7067–7076.

(14) Schäfer, H.; Eisenmann, B.; Müller, W. Zintl Phases: Transitions between Metallic and Ionic Bonding. *Angew. Chemie Int. Ed. English* **1973**, *12* (9), 694–712.

(15) *Chemistry, Structure, and Bonding of Zintl Phases and Ions*; Kauzlarich, S. M., Ed.; VCH Publishers: New York, 1996.

(16) Ramarao, S. D.; Singh, A. K.; Subbarao, U.; Peter, S. C. An Overview on the Structural Diversity of Europium Based Ternary Intermetallics. *J. Solid State Chem.* **2020**, *281* (November 2019), 121048.

(17) Khatun, M.; Stoyko, S. S.; Mar, A. Quaternary Arsenides $ACdGeAs_2$ (A= K, Rb) Built of Ethane-Like Ge_2As_6 Units. *Inorg. Chem.* **2014**, *53* (14), 7756–7762.

(18) Liu, X. C.; Pan, M. Y.; Xia, S. Q.; Tao, X. T. $Sr_{14}Sn_3As_{12}$ and $Eu_{14}Sn_3As_{12}$: Enantiomorph-like Zintl Compounds. *Inorg. Chem.* **2015**, *54* (18), 8875–8877.

(19) Wilson, D. K.; Saparov, B.; Bobev, S. Synthesis, Crystal Structures and Properties of the Zintl Phases Sr_2ZnP_2, Sr_2ZnAs_2, A_2ZnSb_2 and A_2ZnBi_2 (A = Sr and Eu). *Zeitschrift fur Anorg. und Allg. Chemie* **2011**, *637* (13), 2018–2025.

(20) Chen, C.; Xue, W.; Li, S.; Zhang, Z.; Li, X.; Wang, X.; Liu, Y.; Sui, J.; Liu, X.; Cao, F.; et al. Zintl-Phase Eu_2ZnSb_2: A Promising Thermoelectric Material with Ultralow Thermal Conductivity. *Proc. Natl. Acad. Sci. U. S. A.* **2019**, *116* (8), 2831–2836.

(21) Canfield, P. C.; Kong, T.; Kaluarachchi, U. S.; Jo, N. H. Use of Frit-Disc Crucibles for Routine and Exploratory Solution Growth of Single Crystalline Samples. *Philos. Mag.* **2016**, *96* (1), 84–92.

(22) Bruker (2019) APEXII (Version 2019.1) and (2016) SAINT (Version 8.37a). Bruker AXS Inc.: Madison, Wisconsin, USA.

(23) Blessing, R. H. An Empirical Correction for Absorption Anisotropy. *Acta Cryst. A* **1995**, *51*, 33–38.

(24) Sheldrick, G. M. SADABS (2016) Version 2016/2 “Siemens Area Detector Absorption Correction.” Universitat Gottingen:Gottingen, Germany.

(25) Shldrick, G. M. SHELXTL. Bruker AXS Inc.: Madison, Wisconsin, USA 2002.

(26) Bruker (2019) APEX3 (Version 2017.3) and (2016) SAINT (Version 8.37a). Bruker AXS Inc.: Madison, Wisconsin, USA.

(27) Sheldrick, G. M. SHELXT. Universitat Gottingen: Gottingen, Germany. 2014, p Private Communication.

(28) Sheldrick, G. M. SHELXL2018/3. Universitat Gottingen: Gottingen, Germany. 2018.

(29) Toby, B. H.; Von Dreele, R. B. GSAS-II: The Genesis of a Modern Open-Source All Purpose Crystallography Software Package. *J. App. Crystal.* **2013**, *46* (2), 544–549.

(30) Nikolo, M. Superconductivity: A Guide to Alternating Current Susceptibility Measurements and Alternating Current Susceptometer Design. *Am. J. Phys.* **1995**, *63* (1), 57–65.

(31) Vogel, R.; Schuster, H. KHgAs (Sb) Ud KZnAs - Ternare Verbindungen Mit Modifizierter Ni_2In-Struktur. *Z. Naturforsch., B J. Chem. Sci.* **1980**, *35*, 114–116.

(32) Liu, X. C.; Lin, N.; Wang, J.; Pan, M. Y.; Zhao, X.; Tao, X. T.; Xia, S. Q. $Ba_{13}Si_6Sn_8As_{22}$: A Quaternary Zintl Phase Containing Adamantane-like $[Si_4As_{10}]$ Clusters. *Inorg. Chem.* **2013**, *52* (20), 11836–11842.

(33) Klein, J.; Eisenmann, B. Dimere Zintl-Anionen $[Sn_2As_6]^{10-}$ Und $[Sn_2Sb_6]^{10-}$ in Alkaliverbindungen. *Zeitschrift fur Krist. - Cryst. Mater.* **1991**, *196* (1–4), 213–229.

(34) Eisenmann, B.; Klein, J. Zintl-Phasen Mit Schichtanionen: Darstellung Und Kristallstrukturen Der Isotypen Verbindungen $SrSn_2As_2$ Und $Sr_{0.87}Ba_{0.13}Sn_2As_2$ Sowie Eine Einkristallstrukturbestimmung von KSnSb. *Z. anorg. allg. Chem.* **1991**, *598* (1), 93–102.

(35) Eisenmann, B.; RoBler, U. Pniktogenidostannate(IV) Mit Isolierten Tetraeder-Anionen : Neue Vertreter $(E1)_4(E2)_2[Sn(E15)_4]$ (Mit E1 = Na, K; E2 = Ca, Sr, Ba; E15 = P, As, Sb, Bi) Vom $Na_6[ZnO_4]$-Typ Und Die Uberstrukturvariante Vo. *Z. anorg. allg. Chem.* **2000**, *626*, 1373–1379.

(36) Lam, R.; Mar, A. The Metallic Zintl Phase $Ba_3Sn_4As_6$. *Solid State Sci.* **2001**, *3* (4), 503–512.

(37) Lee, K.; Kaseman, D.; Sen, S.; Hung, I.; Gan, Z.; Gerke, B.; Pöttgen, R.; Feygenson, M.; Neuefeind, J.; Lebedev, O. I.; et al. Intricate Short-Range Ordering and Strongly Anisotropic Transport Properties of $Li_{1-x}Sn_{2+x}As_2$. *J. Am. Chem. Soc.* **2015**, *137* (10), 3622–3630.

(38) Hermann, R. P.; Grandjean, F.; Kauzlarich, S. M.; Jiang, J.; Brown, S.; Long, G. J. A Europium-151 Mössbauer Spectral Study of $Eu_{14}MnP_{11}$, $Eu_{14}MnAs_{11}$, and $Eu_{14}MnSb_{11}$. *Inorg. Chem.* **2004**, *43* (22), 7005–7013.

(39) Ernet, U.; Müllmann, R.; Mosel, B. D.; Eckert, H.; Pöttgen, R.; Kotzyba, G. Magnetic Hyperfine Interactions in the Zintl Phase EuZnSn. *J. Mater. Chem.* **1997**, *7* (2), 255–257.

(40) Gerke, B.; Schwickert, C.; Stoyko, S. S.; Khatun, M.; Mar, A.; Pottgen, R. Magnetic Hyperfine Field Splitting in $EuAg_4As_2$ and $EuAg_4Sb_2$. *Solid State Sci.* **2013**, *20*, 65–69.

(41) Ryan, D. H.; Bud'ko, S. L.; Hu, C.; Ni, N. Magnetic and Structureal Transitions in

$EuAg_4As_2$ Studied Using ^{151}Eu Mossbauer Spectroscopy. *AIP Adv.* **2019**, *9*, 125050.

(42) Radzieowski, M.; Stegemann, F.; Klenner, S.; Zhang, Y.; Fokwa, B. P. T.; Janka, O. On the Divalent Character of the Eu Atoms in the Ternary Zintl Phases $Eu_5In_2Pn_6$ and Eu_3MAs_3 (Pn = As-Bi; M = Al, Ga). *Mater. Chem. Front.* **2020**, *4*, 1231–1248.

(43) Lees, J. K.; Flinn, P. A. Mössbauer Effect in Tin Compounds: Interpretation of Isomer Shifts and Determination of the Nuclear Radius Change In112Sn. *J. Chem. Phys.* **1968**, *48* (2), 882.

(44) Gray, P. R.; Farha, F. E. A Mössbauer Investigation of a Platinum-Tin Paraffin Dehydrogenation Catalyst. In *Mössbauer Effect Methodology*; Gruverman, I. J., Seidel, C. W., Eds.; Springer: New York, 1976; pp 47–68.

(45) Liu, K.; Wu, X. W.; Ahn, K. H.; Sulchek, T.; Chien, C. L.; Xiao, J. Q. Charge Ordering and Magnetoresistance in $Nd_{1-X}Ca_xMnO_3$ Due to Reduced Double Exchange. *Phys. Rev. B* **1996**, *54* (5), 3007–10.

(46) Yang, D.; Lampronti, G. I.; Haines, C. R. S.; Carpenter, M. A. Magnetoelastic Coupling Behavior at the Ferromagnetic Transition in the Partially Disordered Double Erovskite La_2NiMnO_6. *Phys. Rev. B* **2019**, *100*, 014304.

For Table of Contents Only:

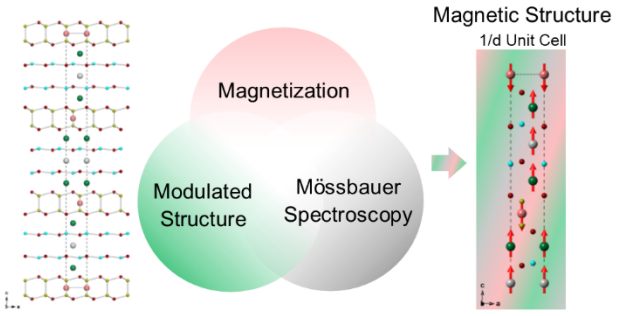

The combination of a detailed analysis into the modulated structure, magnetization properties, and Mössbauer spectroscopy of the $Eu_{11-x}Sr_xZn_4Sn_2As_{12}$ solid solution results in a magnetic model consistent with the unusual magnetic properties of this quinary Zintl phase.